# Atomic processing of optically carried RF signals

Jean-Louis Le Gouët, Fabien Bretenaker, Ivan Lorgeré

Contribution to Volume 54 of *Advances in Atomic, Molecular and Optical Physics.*

# Atomic processing of optically carried RF signals

Jean-Louis Le Gouët, Fabien Bretenaker, Ivan Lorgeré

*Laboratoire Aimé Cotton, CNRS UPR3321,*
*bâtiment 505, campus universitaire,*
*91405 Orsay Cedex, France*

*Corresponding author email :* jean-louis.legouet@lac.u-psud.fr

Abstract : Rare earth ions embedded in crystals are natural high-quality-factor resonators that can be used for processing optically-carried broadband radio-frequency signals. This chapter focuses on the radio-frequency spectrum analysis function and describes different architectures that are designed to reach tens of gigahertz instantaneous bandwidth with sub-megahertz resolution. Various approaches are considered. The active material may act as a spectral buffer memory. Instead one may store a processing function inside the crystal. The latter may then operate either as a frequency-to-angle converter or a frequency-to-time transformer. All those architectures have been explored experimentally. To meet the specific requirements of these processors, frequency agile lasers have been developed. These keynote devices are described in detail.

## 1. Introduction

When absorbing centers are embedded in a host matrix and the medium is cooled to a few degrees Kelvin, homogeneous absorption line widths are dramatically reduced as a result of strongly diminished environmental fluctuations. While the cooling decreases the homogeneous widths, it has little effect on the inhomogeneous line width that results from the static interaction of the absorbing centers with the host. When exposed to monochromatic

light, the material is excited only within the homogeneous-width of the incoming light and a narrow spectral hole is burned at this position within the absorption profile [1]. This work is part of a long quest for practical applications of spectral hole burning (SHB) in solid materials, an effort that has been pursued since the beginning of the 70's.

The first application considered was optical memory, with the goal of overcoming the storage density diffraction limit by adding a fourth non-spatial dimension, namely frequency, to the memory volume. The initial two patents in this area consider page-oriented storage, where a spatial page of information is stored at a spectral address [2], [3]. To retrieve information one tunes the readout laser to the engraving wavelength. After discovery of permanent SHB in organic materials [4], [5], storage of 2000 [6], 6000 [7] and ultimately 10000 images [8] was demonstrated in chlorine, a porphyrine derivative. A storage density of up to 10Gb/cm² is reached at a temperature of 1.7K by the ETH group [9]. Transfer rate is then limited by the inverse spectral channel width. Time domain encoding of data address can be substituted for spectral addressing [10]. In this approach the Fourier transform of the data sequence is engraved over the inhomogeneously broadened spectral memory absorption band. Then, one has simultaneous access to all the spectral channels. More precisely the data transfer rate equals the inhomogeneous linewidth, a figure that reaches tens of GHz in rare earth ion doped materials such as $Tm^{3+}$:YAG. This excessively high speed proves difficult to manage and a hybrid chirped carrier technique is proposed. Combining temporal encoding with spectral scan, one has an approach that conveys flexibility to data transfer at both engraving and readout [11] [12] [13]. Despite excellent performance in terms of storage density and capacity, access time and transfer rate, SHB memories suffer from operating at liquid helium temperature, a severe limitation for mass market application.

In the quest of niches for SHB technology, it was soon realized that the specific time/frequency dimension should not be considered on an equal footing with the spatial ones,

as it was in large memory application. Instead, the inhomogeneous linewidth can be regarded as the spectral bandwidth of an optically carried signal analog processor. In this respect SHB materials can outdo any existing electronic processor and appear to be potentially attractive microwave photonics components, offering an instantaneous bandwidth in excess of 10GHz with a channel capacity larger than $10^4$.

Application to range and Doppler processing of RADAR return signals has been proposed recently. The cross-correlation function of the encoded RADAR pulse and the return signal is stored as a spectral grating within the SHB material. Even if the pulse encoding is renewed at each transmission, the correlation grating remains unchanged and can be accumulated for milliseconds. Scanning a monochromatic laser through the engraved spectral structure and using a narrow band detector one may retrieve information on target distance and speed with large dynamic range [14]. Another application has been considered for array antennas. For narrow band operation, one directs the gain to the target by adjusting the relative phase shift of the array elements. The phase shift procedure fails to provide an achromatic delay between the array elements in broad band operation, giving rise to the so called “squint effect”. Then “true time delays” can be stored in a SHB material and be applied to arbitrary waveform optically carried signals without latency, either at transmission or reception [15] [16] [17].

Broadband devices are also needed for spectral analysis at the back-end of the heterodyne receivers used in (sub)millimeter astrophysics. The molecular lines observed in astrophysics are generally broadened by either the Doppler effect in the interstellar medium or by pressure in planet atmospheres. In the former case, a 1000km/s-wide spectral window is generally enough to analyze a 700km/s Doppler broadening. If at 100GHz this interval is covered by a 330MHz bandwidth spectrometer, the required bandwidth raises to 10GHz at 3THz, the position of the HD line, and 20GHz at 6THz, the position of the atomic oxygen

narrow line. As for the lines observed in planetary atmospheres, their pressure broadening may reach several GHz and they often exhibit a narrow feature at their center, corresponding to high altitude emission. Both the broad global profile and the narrow central structure usually need be explored. In an heterodyne receiver, the THz range signal, mixed with a local oscillator, is shifted down to the GHz range where its spectral analysis is usually performed either by acousto-optic spectrometers (AOS) or by digital auto-correlators (DAC). The AOS cover a bandwidth of up to 2GHz in a single unit. The DAC offer a smaller bandwidth but their flexible resolution can accommodate fine details such as narrow lines in the dark clouds of our galaxy, with Doppler broadening as small as 0.1-1km/s.

Combining more than 10GHz instantaneous bandwidth with less than 1MHz resolution, SHB materials have the potential to accomplish a breakthrough in RF spectral analysis. In addition they would offer improved power consumption with respect to DAC's together with resolution flexibility and better stability than AOS's. In this paper we review recent experimental achievements that demonstrate SHB capabilities for broadband spectral analysis with a unity probability of intercept. Different approaches have been considered. Some use the SHB material as a storage medium where the optically carried RF signal spectrum is accumulated before readout. Unlike this "spectral photography" scheme, other approaches avoid the storage of the signal under investigation in the SHB medium. Instead the material is programmed as an analog processor that continuously processes the signal-carrying beam. Various programming functions have been explored. Indeed the SHB material is opened to a wealth of wideband spectrum analysis architectures through diverse combinations of space and frequency variables.

After a brief review of conventional RF spectrum analysis techniques in Section 2, we present the spectrum photography architecture in Section 3. Although this is the most recently considered approach it is also the conceptually simplest one. Then we introduce the

programmable filtering approach in section 4, reestablishing the mathematical expression of the SHB material optical response within the framework of a two-level atom ensemble picture. Two demonstrations of analog RF signal processing are then presented in Sections 5 and 6. One processor – the rainbow analyzer – achieves the angular separation of the spectral components while the other one – the photon echo chirp transform analyzer – displays the angular components in the time domain. Keystones of these architectures, specific lasers had to be developed for these experiments. Section 7 is devoted to these devices.

## 2. Radio frequency spectral analyzers

In this section we review the RF spectrum analyzers that have been considered so far for spatial missions. They have been used at the back end of heterodyne receivers for atmospheric and astronomic observation in the submillimeter and millimeter wavelength range. The THz signal collected by the antenna is mixed with a local oscillator, which shifts its frequency to the GHz range. After amplification the signal is then directed to various RF spectrum analyzers that may include filter banks, acousto-optic analyzers, digital and analog autocorrelators, and surface acoustic wave devices.

In a filter bank analyzer the signal is divided into different spectral channels, each being equipped with its own bandpass filter and detector. Weight and power consumption limits the channel number to a few tens. Bandwidth and resolution are fixed. Missions devoted to solar and atmospheric observation carry those devices [18] [19], each filter bank covering a specific molecular line, with optimum resolution at the line center [20] [21].

Acousto-optic spectral analyzers (AOS) may offer up to 2GHz instantaneous bandwidth in a single compact and low consumption unit. First demonstrated in the 70's [22] [23], these analyzers were used for the first time in a civilian space mission in 1998 [24] [25] [26]. The ODIN satellite [27], launched in 2001, carries an AOS with 1000 channel resolution over 1GHz bandwidth [28]. The forthcoming HERSCHEL mission [29] will also be equipped

with AOS [30] [31] [32]. In an AOS the RF signal to be analyzed is fed to the transducer of an AO modulator. The acoustic wave generates an index grating that diffracts a monochromatic laser beam. The different spectral components of the RF signal give rise to different grating components that diffract the beam in different directions. Diffracted intensity distribution along a photodetector array then reflects the RF signal power spectrum.

Since the Wiener-Khinchin theorem relates the power spectrum to the autocorrelation function, one may record the latter quantity and then retrieve the power spectrum by Fourier transform computation. The quantity to be measured is the time averaged product of the signal and its time delayed replica, at various settings of the time delay. The inverse time delay half size and the number of delay settings respectively determine the analyzer bandwidth and channel number.

In a digital autocorrelator the signal is first processed by an analog to digital converter (ADC). Because of time averaging a poor dynamic range converter can result in excellent dynamic range autocorrelation measurement [33] [34]. Digital processing offers numerous benefits such as stability and absence of additional noise. Delays, supplied by cascaded shift registers, are easily controlled through the clock rate, which gives resolution flexibility. Finally the device is easy to assemble and reproduce [35]. Limitation comes from the sampling rate of the ADC. With a 2GS/s rate (GS/s = Gigasamples/second), available units can offer up to 1GHz bandwidth [36]. Another important limitation is set by power consumption that grows with the bandwidth. ODIN and HERSCHEL missions are equipped with such devices [27] [29] [37] [38].

Increased bandwidth is made available in analog auto-correlators. In these devices two signal replica counter-propagate along two parallel micro-strip lines. The two traveling waves are sampled at taps, evenly spaced along the lines. Different pairs of opposite taps supply different delays between the sampled signals that are subsequently multiplied and digitally

converted [39] [40]. The most advanced system offers an instantaneous bandwidth of 4GHz and 128 channels. Signal attenuation along the microstrips limits the available delay and thus the spectral resolution.

High resolution broadband spectral filtering and large delay generation are tasks that are difficult to achieve with pure electronic means. Hybridizing may help to address these issues as already illustrated by the AOS where optics is combined with electronic processing. Another example of hybridizing is offered by surface acoustic wave (SAW) dispersion lines. By converting the electric signal into a surface acoustic wave one reduces both the wavelength and the delay line dimension in the ratio of sound and light speeds. With the small size acoustic resonant circuits and delay lines that are readily feasible one can build dispersion lines with large group delay dispersion rate. Multiplication by a chirped reference followed by dispersion in the appropriate SAW line performs the signal "*chirp transform*" [41] and results in the desired power spectrum profile [42] [43]. The device to be placed in The Stratospheric Observatory For Infrared Astronomy (SOFIA) will cover 205MHz with 50kHz resolution and 40dB dynamic range [44] [45] [46] [47].

The features of these RF spectrum analyzers are summarized in Table 1.

| | Filter bank | Digital Autocorrelator | Analog autocorrelator | SAW | AOS |
|---|---|---|---|---|---|
| Bandwidth | 1.2GHz | 700MHz | 3.6GHz | 205MHz | 1GHz |
| Channel number | 25 | 100 | 128 | 4096 | 2000 |
| Dynamic range | 60dB | 48dB | 38dB | 40dB | 30dB |
| Spectral flexibility | no | yes | no | no | No |
| Best resolution | NA | 140kHz | NA | NA | NA |
| Interception probability | 100% | 100% | 100% | 100% | 100% |
| Access time | FT limited | Integration time | Integration time (>10ms) | FT limited | Readout time |

Table 1. Features of current RF spectrum analyzers for sub-millimeter astronomy applications

# 3. Spectrum photography architecture

## 3.1. Principle of operation

Although it has been considered only recently [48]-[52]], the spectrum photography architecture is actually the simplest of the three architectures we consider here. It consequently constitutes a good introduction to more complicated schemes which will be discussed later. Its principle of operation can be understood as a two-step process from the scheme of Figure 1.

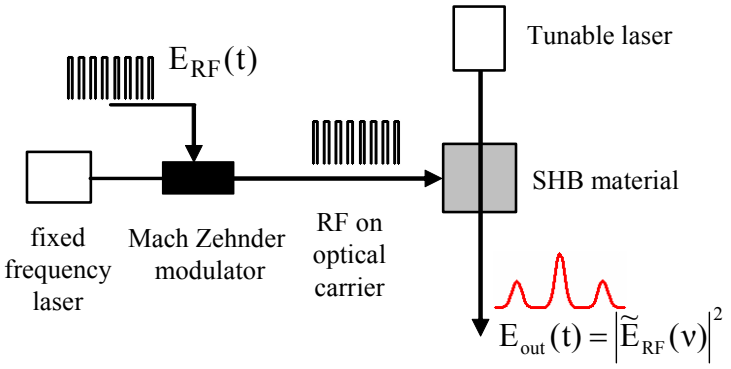


Figure 1. Basic principle of the spectrum photography analyzer.

The RF signal to be analyzed is transposed on a monochromatic fixed frequency laser beam with the help of a Mach-Zehnder modulator. The laser frequency is adjusted in such a way that one of the RF-signal-carrying side-bands lies inside the SHB material absorption band. [see Figure 2(a)]. Upon crossing the SHB material, the beam excites the ions that are resonant with the different optically carried spectral components of the RF signal. Consequently, the optically carried RF spectrum is recorded in the material absorption spectrum [see Figure 2 (b)]. By probing the material transmission with a frequency chirped laser [see Figure 2 (c)] one readily obtains a temporal image of the engraved spectrum [see Figure 2 (d)]. Although the read out scanning procedure is reminiscent of usual electronic spectrum analyzers, the SHB analyzer exhibits a very distinctive feature. Indeed, although spectral addresses are probed sequentially the RF signal is continuously recorded in the SHB material that operates as a spectral buffer

memory. By simply using two separate lasers for engraving and probing one may reach 100 % probability of interception. Storage lifetime in the buffer memory is limited by the excited level population lifetime that can exceed 10ms in the materials we consider. The spectral resolution is limited by the laser noise and the square root of the chirp rate of the reading laser. Given the broad bandwidth to be scanned in less than 10ms, the chirp rate limited resolution will dominate the homogeneous linewidth of the optical transition. The geometry of the experiment can be rather simple, allowing us to consider this experiment as an elementary pixel of a future broadband spectrally resolved RF imaging system.

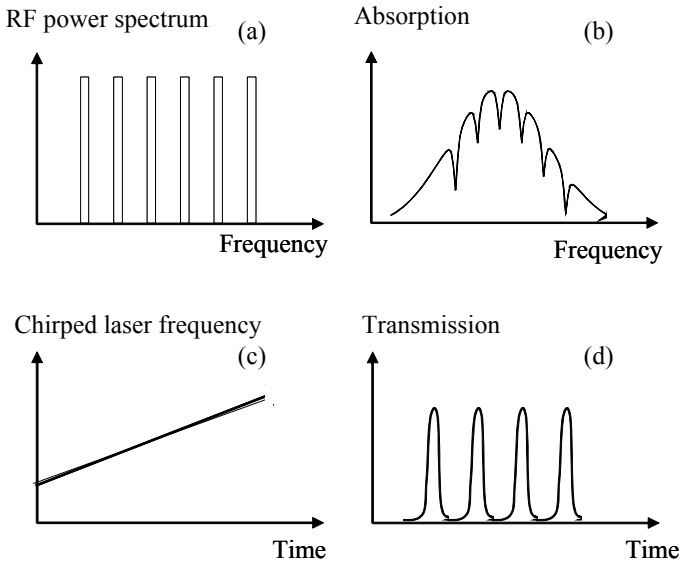


Figure 2. Basic steps of the spectrum photography analyzer. The RF spectrum (a) is engraved in the absorption spectrum (b) which is then read by a frequency-swept laser (c) leading to signal (d).

The principle schematized in Figure 1 has been implemented experimentally. This experiment makes use of a particular type of SHB material, namely a $Tm^{3+}$:YAG crystal. Before describing this experiment we turn to a short summary of the basic properties of rare earth doped crystals for SHB, with $Tm^{3+}$:YAG as an illustration.

## 3.2. Basic spectroscopic properties of $Tm^{3+}$:YAG for SHB experiments

Rare earth ion-doped crystals (REIDC) represent a satisfactory candidate for high resolution applications. The common structure of rare earth atoms is $5s^2 5p^6 4f^{n+1} 6s^2$, where $0 \leq n \leq 13$. In

triply charged ions, one 4f electron and both 6s electrons are removed. Optical transitions within the $4f^n$ configuration are forbidden for parity reason. Nevertheless some weak lines, with oscillator strength of the order of $10^{-8}$, result from mixing with the $4f^{(n-1)}5d$ configuration in sites without inversion symmetry. In addition the sharpness of the lines is preserved, in a solid state matrix, by the shielding of 4f electrons by the 5s and 5p electrons. At $5^{\circ}K$ in a crystal host matrix the homogeneous linewidth is usually much smaller than 1MHz. If profitable as far as spectral resolution is concerned, a weak oscillator strength unfortunately means that a larger amount of energy is needed for engraving.

On some transitions the ions behave as two-level atoms, with an excited state that directly decays to the ground state. Then the spectral hole lifetime coincides with that of the excited state. The $^4I_{13/2} \leftrightarrow {}^4I_{15/2}$ transition of $Er^{3+}$ near 1.5μm belongs to this class. It offers a 10ms storage time in the upper level [53]. This material gives access to the wealth of tools that has been developed for fiber-optics communications, including versatile lasers and amplifiers [54].

Different processes may slow down the return to initial state and the spontaneous erasure of the engraved structure. In $Eu^{3+}$ and $Pr^{3+}$ doped crystals, resonant excitation results in an optical pumping alteration of the atom distribution over the ground state hyperfine structure [55]. This alteration may survive for hours before return to thermal equilibrium. The long memory life is obtained at the expense of the bandwidth. Indeed the lines connected to the different hyperfine sublevels overlap, which limits the available bandwidth to a few MHz.

A hyperfine-structure-free-ion, such as Thulium $Tm^{3+}$ is preferred for our broadband processing application. . On the $^3H_4 \leftrightarrow {}^3H_6$ transition in $Tm^{3+}$ doped crystals, a bottleneck metastable state, with a lifetime of about 10ms, delays the excited state decay to the ground state [56] (see Figure 3). The $^3H_4 \leftrightarrow {}^3H_6$ transition wavelength at 793nm is compatible with integrated electro-optic $LiNbO_3$ ultrafast modulators. This wavelength also falls within the range of common semiconductor lasers and of the Titanium-Sapphire laser. Optical pumping

from the ground state to the bottleneck state $^3F_4$ via the upper state $^3H_6$ offers a convenient way to accumulate engraving [57]. Owing to the 500µs lifetime of the upper level, an optical pumping cycle lasts about 1ms. Several cycles can take place during the 10ms lifetime of $^3F_4$. We experimentally verified that a large fraction of the ground state population can actually be transferred to $^3F_4$. This procedure entails two benefits. First optimal engraving can be reached without saturating the $^3H_4 \leftarrow {}^3H_6$ transition, which means lower laser intensity requirements. Second, with a 1kHz refresh rate and a 10ms storage lifetime, the diffraction efficiency is nearly stationary.

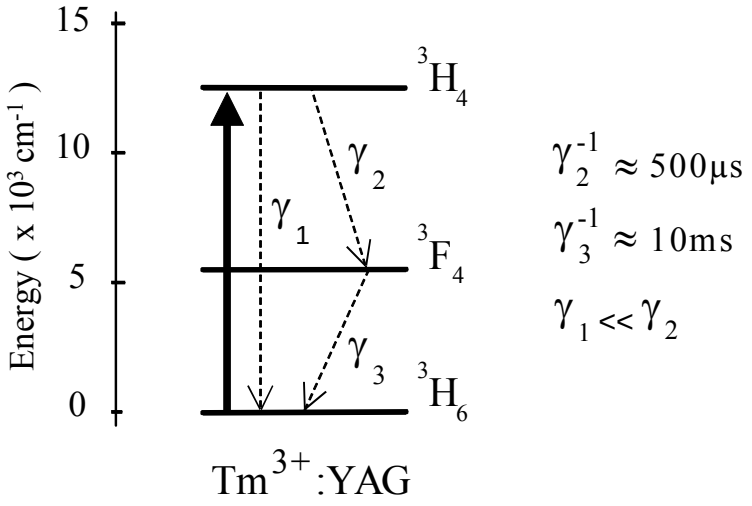


Figure 3. Level scheme in $Tm^{3+}$: YAG. The laser is coupled to the $^3H_4 \leftrightarrow {}^3H_6$ transition at 793nm. The level decay rates are denoted by $\gamma_i$.

## 3.3. Experimental demonstration

### 3.3.1. Collinear experiment

The experimental demonstration of the spectrum photography architecture has been first performed using the experiment schematized in Figure 4 [51]. A very similar experiment has been performed at the University of Colorado [52]. The experiment reported in [51] is based on a 2.5-mm long 0.5-at. % doped $Tm^{3+}$:YAG crystal cooled to 4.5 K. Under these conditions, the peak absorption at 793 nm is 85 %.

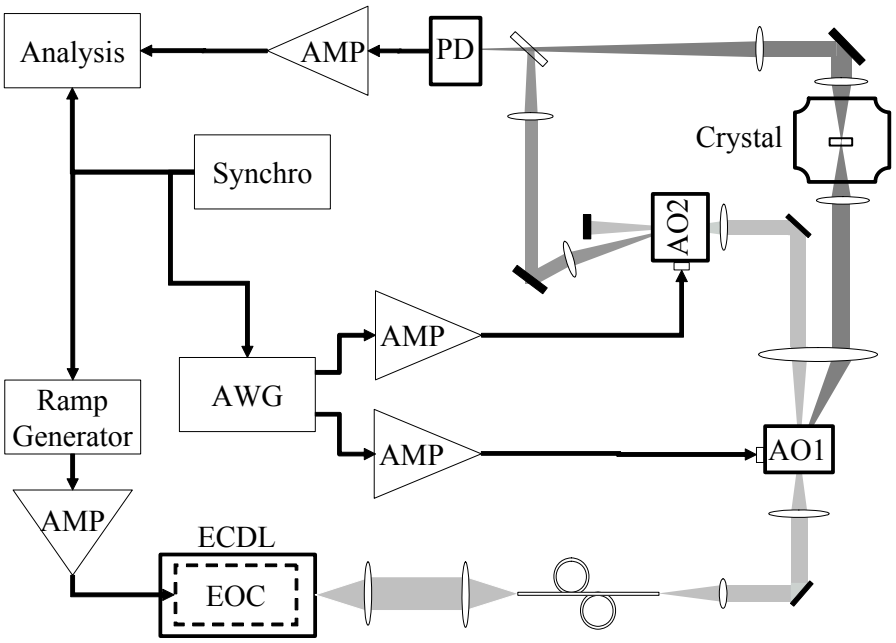


Figure 4. Collinear spectrum photography analysis experiment.

As can be seen in Figure 4, this proof of principle experiment has been performed with only one laser. This laser is a frequency agile external cavity diode laser (ECDL) [58]. It is used alternatively as the engraving laser and as the probe laser of Figure 1. During the engraving stage, the frequency of this laser is tuned by steps to different spectral positions, which mimics an optically carried RF signal. The power of the beam is controlled by the acousto-optic modulator AO1 and is focused to a waist radius $w_0$ = 90 µm inside the crystal. The zeroth-order beam at the output of AO1 can be frequency shifted using AO1 before being mixed with the beam emerging from the cryostat. This allows performing a heterodyne detection at 5 MHz of the light emitted by the ions, as will be illustrated later. Light is detected using a PIN photodiode (PD) followed by a 10-dB gain amplifier.

An example of a 10-GHz bandwidth spectral analysis is reproduced in Figure 5. The engraved spectrum consists of a series of 16 spikes each lasting 150 µs (pulse energy 450 nJ) with the laser tuned to 16 different frequencies. The reading is performed 1.6 ms later, with a 10-GHz bandwidth scanned in 2 ms. During the reading phase, one reduces the optical power

incident on the crystal to 750 μW, in order not to erase the engraved spectrum. The resulting signal is demodulated and its amplitude is normalized to the unsaturated transmission of the crystal. Among the 16 engraved peaks, 15 are equally spaced by 620 MHz all over the 10-GHz bandwidth [see Figure 5 (a)]. In this experiment, the 16$^{th}$ engraved peak is located 5 MHz apart from one of the 15 equally separated peaks. This doublet is perfectly resolved by our analyzer, as can be seen in Figure 5 (b). The linewidth of each peak corresponds to 2 MHz in this experiment.

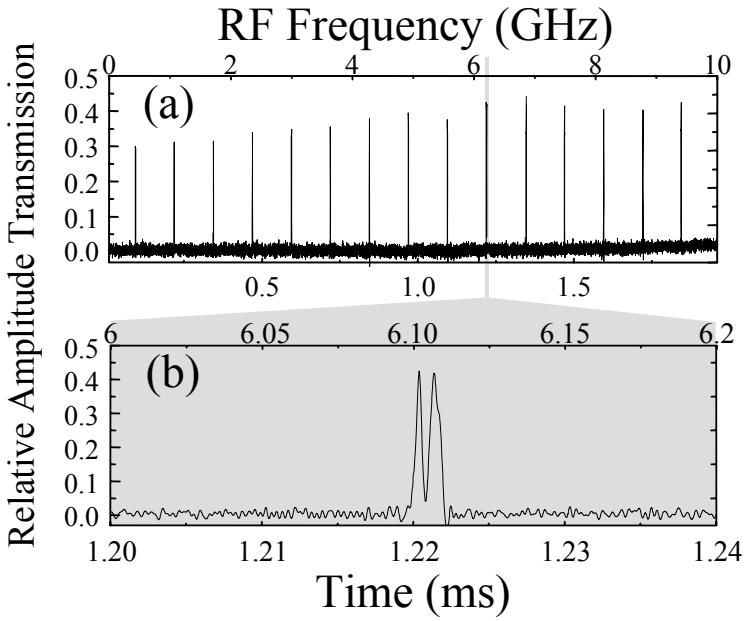


Figure 5. (a) Example of spectrum obtained using the setup of Figure 4. The 10-GHz bandwidth readout is performed in 2 ms. 15 equally spaced tones have been engraved in the sample, except for a 5 MHz doublet, which is perfectly resolved as can be seen in (b).

Of course, this resolution depends on the chirp rate $r$, as can be seen from the experimental results reproduced in Figure 6. The open circles in Figure 6 represent the measured evolution of the width of a single peak engraved in 200 μs (pulse energy 600 nJ) versus the reading chirp rate. Indeed, it is well known [60] that as soon as the width $\Gamma/2\pi$ of any spectral feature of interest is not much larger than $r^{1/2}$, the readout gets distorted and, in particular, broadened. If we consider a Lorentzian lineshape of width $\Gamma/2\pi$ (in Hz) probed by a light beam of varying detuning $\delta(t) = rt$

(exact resonance occurs at $t = 0$), the resulting time evolution $s(t)$ of the transmitted field amplitude normalized to the undistorted one is given by [61]:

$$s(t) = \mathrm{Im}\left\{ \frac{\Gamma}{\sqrt{r}} \frac{1+i}{2\sqrt{2}} \mathrm{e}^{-\frac{i}{4\pi r}(\Gamma - 2i\pi r t)^2} \mathrm{erfc}\left[ \frac{1-i}{2\sqrt{2}} \frac{1}{\sqrt{\pi r}} (\Gamma - 2i\pi r t) \right] \right\}, \quad (1)$$

where erfc stands for the complementary error function. This equation leads to the thick line of Figure 6 obtained with $\Gamma/2\pi = 700$ kHz, which is in very good agreement with the measurements. This value of $\Gamma/2\pi$ is larger than the absolute limit given by twice the homogeneous linewidth of the ions at 4.5 K (2x150 kHz = 300 kHz) because of the contribution of the laser frequency jitter, which will be shown in Section 7.3. This limit linewidth $\Gamma/2\pi$ becomes relevant when it is larger than $r^{1/2}$ whose value is reproduced as a thin line in Figure 6. This shows that a sub-MHz resolution can be reached if the 10 GHz bandwidth is probed in 10 ms, leading to a number of independent frequency bins equal to 10000. Of course, due to the finite lifetime of the engraved spectrum that is limited by the lifetime of the metastable level population (10 ms), the use of a slower chirp in order to improve the frequency resolution and to reach a number of frequency channels equal to 10000 will lead to an increase of the delay before the engraved spectrum is read and hence to a reduction of the detected signal.

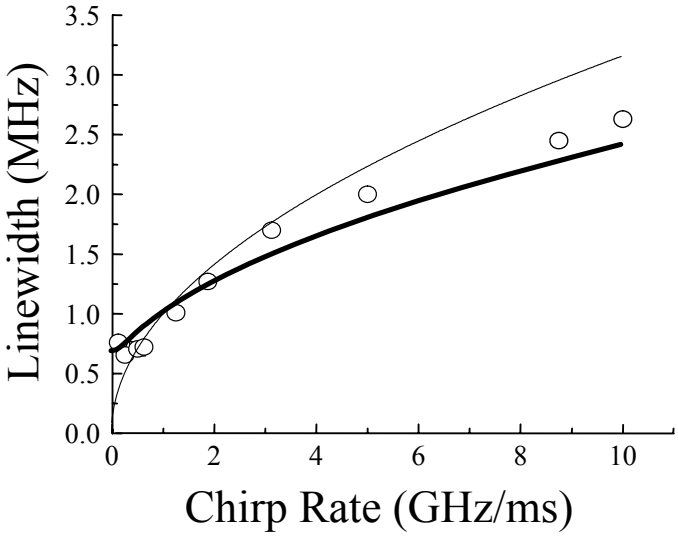


Figure 6. (a) Experimental (circles) and theoretical (thick line) evolutions of the linewidth (full width at half maximum) of a single-frequency readout signal versus chirp rate $r$. The thin line is $r^{1/2}$.

Another important property of a spectrum analyzer is its dynamic range. It can be extracted from the experimental results reproduced in Figure 7. This figure represents the evolution of single peak readout amplitude versus engraving optical energy. The experimental points have been obtained for two values of the engraving pulse duration (400 µs and 600 µs) and by varying the engraving power. The engraved peak is read after a time delay equal to 1.3 ms. These measurements exhibit a typical saturation behavior, which can be reproduced from a simple three-level rate equation description of the system represented as a full line in Figure 7.

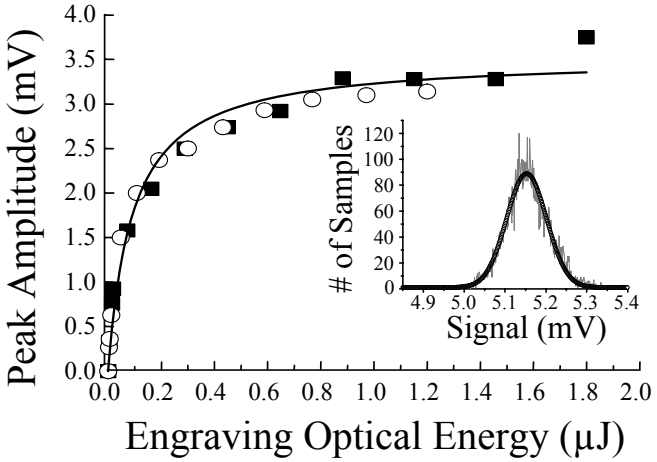


Figure 7. Experimental (circles and squares) and theoretical (full line) evolutions of the detected amplitude of a peak versus the engraving optical energy. The delay between the engraving and the reading of the peak is 1.4 ms. The engraving times are 400 µs (open circles) or 600 µs (filled squares). The theoretical curve is computed with saturation energy equal to 75 nJ. The inset shows the distribution of the signal value in the background absorption region (thin line) together with a Gaussian fit (thick line) leading to a standard deviation of 50 µV.

We estimate the linear part (with a maximum non-linearity of 20 %) of this response to correspond to a signal voltage between 0 and 2 mV. To compare this signal with the typical signal noise, we record 10333 successive samples separated by 8 ns while the laser is chirped in a region where no peak has been engraved. The inset in Figure 7 then reproduces the distribution of the signal value together with a Gaussian fit. The average value of the signal (5.15 mV) corresponds to the transmitted signal when the absorption is not saturated. The standard deviation of this Gaussian noise is found to be equal to 50 µV. The main components of this noise are i) the thermal noise of the detector and amplifier, due to the low value of the detected optical power (a 750 µW incident power is incident on the crystal during the reading stage) and

ii) the low-frequency components of the laser intensity noise. This leads to a value of 16 dB for the linear dynamic range in terms of optical field amplitude of our "photographic scheme" spectral analyzer. Since in this architecture the field emitted by the atoms is directly proportional to the RF signal power, this corresponds to a 16 dB dynamic range for the RF signal also. This relatively poor value is limited by two factors. First, the signal amplitude is rather low, due to the small number of atoms probed by the optical beams. Second, the noise is rather important, due to the fact that our measurements are performed on a non-dark background. Indeed, in this direct transmission experiment, the peaks of Figure 5 are sitting on a background due to the transmitted laser power. The shot noise associated with this background intensity is actually the limiting factor here. This is why we now turn to the realization of a dark background experiment based on a non-collinear geometry.

3.3.2. Non-collinear experiment

The principle of this non-collinear spectrum photography analyzer is summarized in Figure 8, in comparison with the collinear one which has just been described. Figure 8 (a) represents the writing field $E_W$ impinging on the SHB sample in the collinear experiment. During the read-out phase of this experiment [see Figure 8 (b)], the field with real amplitude $E_P$ probes the susceptibility of the material which has been spectrally shaped during the engraving phase. This susceptibility gives rise to a macroscopic polarization that radiates the field $E_{RF}$, with a real part $E_R$ and an imaginary part $E_I$. Since the two fields are collinear, the detected intensity is given by

$$I = {E_P}^2 + 2E_P E_R + {E_R}^2 + {E_I}^2 \approx {E_P}^2 + 2E_P E_R \,. \qquad (2)$$

In Eq.(2), the intensity of the RF field emitted by the ions has been neglected because it is usually much smaller than the two other terms. This equation perfectly illustrates the pros and cons of the collinear architecture. Indeed, it shows that the term $E_I$, i. e., the dispersive response of the atoms, can be neglected thanks to the homodyning or the real part $E_R$ by the probe field amplitude $E_P$. This leads to the very good frequency resolution of Figure 6. The drawback of this

approach is that the term $E_P{}^2$ is very large and leads to a strong noise which severely limits the signal to noise ratio of the analyzer.

To circumvent this problem, we choose to illuminate the sample with two rather than one engraving beams, as shown in Figure 8 (c). The two engraving beams both carry the same RF signal and are separated by a small angle in the SHB crystal. Consequently, they will engrave a spatial grating only in atoms which are resonant with their spectral components. To read this family of gratings, the chirped probe beam is then incident along the direction of one of the engraving beams, as seen in Figure 8(d). This beam will then be diffracted by the gratings engraved in the spectrum only when it corresponds to an engraved frequency. This is why the RF field $E_{RF}$ emitted by the ions can now be detected on a dark background.

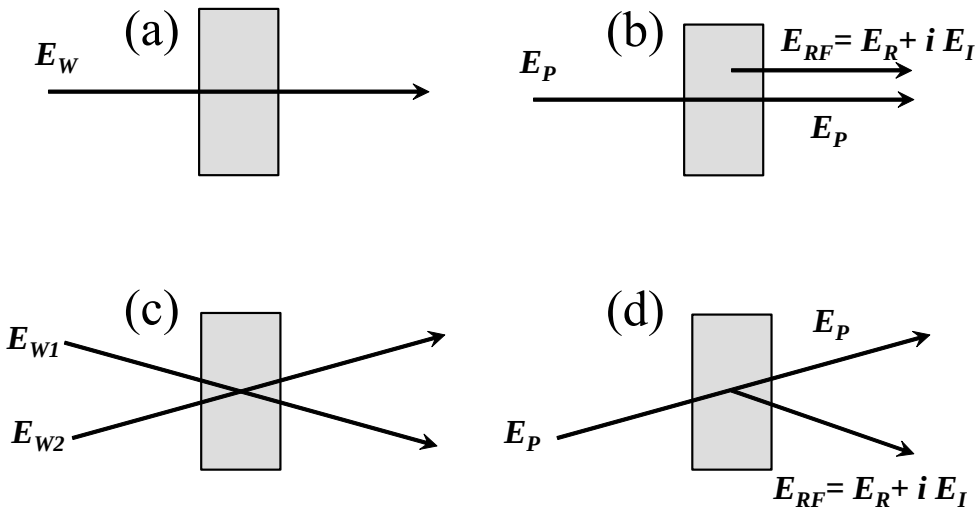


Figure 8. Principle of the (a,b) collinear and (c,d) non-collinear geometries.

The detected intensity is given by

$$I = E_R{}^2 + E_I{}^2 \ . \tag{3}$$

As expected, the probe field intensity and its associated shot noise have disappeared. However, we now have two new problems. First, the detected intensity becomes proportional to the square of the RF power, leading to a decrease of the sensitivity of the analyzer. Second, the system is now sensitive to the imaginary part of the atomic response also. This leads to a strong

degradation of spectral resolution, as illustrated by the experimental result shown in Figure 9 (a). In this figure, one can clearly see that the detection of both quadratures of the emitted field leads to a dispersive-like response of the system. This strongly degrades the spectral resolution of the system. To get rid of the dispersive part of the atomic response, we perform a heterodyne detection of the diffracted beam. To this aim, a fraction of the probe beam is frequency shifted by an acousto-optic modulator operating at frequency *f* and mixed with the diffracted field before it reaches the detector. The detected intensity is given by

$$\begin{aligned} I &= {E_{LO}}^2 + 2E_{LO}E_R\cos(2\pi ft) - 2E_{LO}E_I\sin(2\pi ft) + {E_R}^2 + {E_I}^2 \\ &\approx {E_{LO}}^2 + 2E_{LO}E_R\cos(2\pi ft) - 2E_{LO}E_I\sin(2\pi ft)\ , \end{aligned} \tag{4}$$

where $E_{LO}$ is the local oscillator field amplitude. The detected beat note can be demodulated with the correct phase reference to isolate the term $2E_{LO}E_R$, which contains only the real part $E_R$ of the emitted field. This leads to the experimental result of Figure 9(b). One can see that the dispersive part of the atomic response has been almost perfectly eliminated, in agreement with Eq. (4). According to this equation, one can see that i) the signal intensity is again proportional to the RF signal intensity; ii) the detection no longer occurs on a dark background, due to the presence of the local oscillator intensity. However, the system is now sensitive to the spectral component of the local oscillator intensity noise at frequency *f*, and no longer to the low-frequency part of the intensity noise as in the case of the collinear geometry. A shot-noise limited signal-to-noise ratio is then easier to reach here. Optimization of the signal to noise ratio of the analyzer, i. e. of its linear dynamic range, hence consists in increasing the local oscillator power to increase the signal of Eq. (4), until the total detected power reaches the saturation limit of the detector for the maximum value of the power diffracted by the ions.

Recent results [62], obtained with a 500-µm value for the beam waist inside the crystal, a 10 mW probe beam power, an optimized local oscillator power and a PIN photodiode led to a linear dynamic range approaching 40 dB, together with MHz resolution and 10-GHz bandwidth.

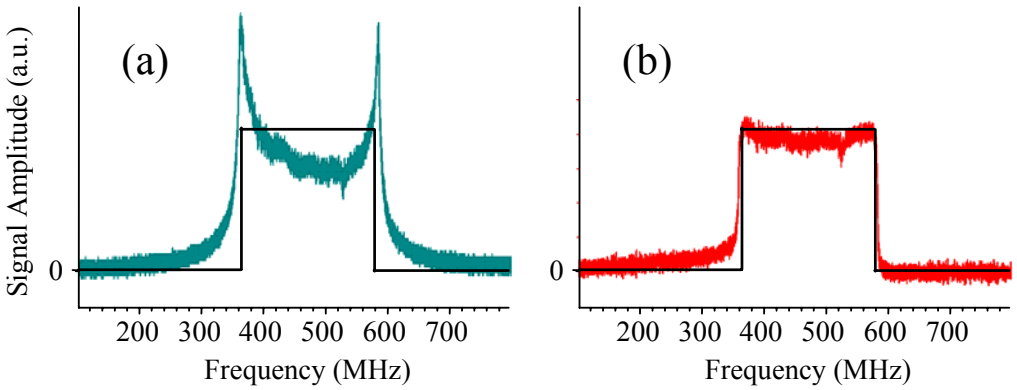


Figure 9. Detected spectrum for the non-collinear experiment. In (a) and (b), the engraved spectrum is represented by the rectangular curve. (a) The total diffracted field is detected. (b) A heterodyne detection permits to isolate the real part of the emitted field and to discard the dispersive part of the atomic response.

# 4. Frequency selective materials as programmable filters

## 4.1. Reconfigurable filtering

In section C the spectrum of the RF signal to be analyzed is stored within the SHB material and is then retrieved through the transmission spectrum of a probe beam. In other words the probe beam is filtered by the SHB medium that has been previously programmed by the optically carried RF signal. With such a representation of the SHB material function one insists on its processing capability. This picture is substantiated by the mathematical expression of the optical response, as established in the pioneering works [10] and [63]. It is shown that the optical signal radiated by a SHB material can be made proportional to a three field product: $\tilde{\mathscr{E}}_1^*(\vec{r},\nu)\tilde{\mathscr{E}}_2(\vec{r},\nu)\tilde{\mathscr{E}}_3(\vec{r},\nu)$ in the spectral domain, the first two fields being involved in the engraving stage while $\tilde{\mathscr{E}}_3(\vec{r},\nu)$ represents the probe field spectral shape. At first sight this is nothing but a trivial third order non-linear optical process. Atomic spectral selectivity makes a difference. In non-linear optics spectral selectivity generally results from phase matching and transparency conditions. In the processes we consider, spectral selectivity is imposed by atomic coherence lifetime. The probe field component $\tilde{\mathscr{E}}_3(\vec{r},\nu)$ at frequency $\nu$

does not interact with the engraved structure $\tilde{\mathcal{E}}_1^*(\vec{r},\nu')\tilde{\mathcal{E}}_2(\vec{r},\nu')$ at separation $\nu'-\nu$ larger than the inverse atomic coherence lifetime. In this section we briefly re-establish this specific behavior within the elementary framework of a two-level atom ensemble.

## 4.2. Linear response

Whatever the medium, response to a probe field $E_3(\vec{r},t)$ is described by the macroscopic polarization density $P(\vec{r},t)$. In the weak field regime the response reduces to the linear component and can be expressed in the frequency domain as

$$\tilde{P}(\vec{r},\nu)=\varepsilon_0\tilde{\chi}(\vec{r},\nu)\tilde{E}_3(\vec{r},\nu)\,, \tag{5}$$

where : $\tilde{f}(\nu)=\int f(t)e^{-2i\pi\nu t}dt$ and $\chi(\vec{r},t)$ represents the electric susceptibility.

In the present work the optical fields interact with an absorbing medium made of resonantly excited two-level atoms. Lower and upper states |a> and |b> are connected by an electric dipole transition whose dipole moment $<a|er|b>$ is denoted by $\mu_{ab}$. The polarization density of such an atomic ensemble is

$$P(\vec{r},t)=N\mu_{ab}\int g(\nu_{ab})\rho_{ab}(\nu_{ab},\vec{r},t)d\nu_{ab}+c.c.\,, \tag{6}$$

where N and $\rho_{ab}(\nu_{ab},\vec{r},t)$ respectively stand for the atom spatial density and for the off-diagonal density matrix element and $g(\nu_{ab})$ represents the atom distribution as a function of the transition frequency. The width of $g(\nu_{ab})$ corresponds to the transition inhomogeneous linewidth.

To relate the general expression (5) with the microscopic description given by Eq. (6) we have to solve the atomic density matrix equation

$$\begin{cases} i\hbar\dot{\rho}=[H,\rho]+i\hbar\left.\dfrac{d\rho}{dt}\right|_{relaxation} \\ \quad H=H_0-er.E(\vec{r},t)\,, \end{cases} \tag{7}$$

where $H_0$ represents the atom Hamiltonian. The relaxation term accounts for the upper state decay to the ground state at rate $\gamma_b$ and for the off-diagonal matrix element $\rho_{ab}$ decay at rate $\gamma_{ab}$. The level population difference $\rho_{aa}-\rho_{bb}$ is denoted by $n_{ab}$. The level populations also satisfy the closure relation, $\rho_{aa}+\rho_{bb}=\mathrm{Tr}(\rho)=1$.

The incident traveling waves are decomposed in their complex components according to

$$E(\vec{r},t)=\frac{1}{2}(\mathscr{E}(\vec{r},t)+\text{c.c.})\,, \tag{8}$$

where the complex field $\mathscr{E}(\vec{r},t)$ is related to the complex amplitude $\mathscr{A}(\vec{r},t)$ by

$$\mathscr{E}(\vec{r},t)=\mathscr{A}(\vec{r},t)\exp\left(2i\pi\nu_0 t\right). \tag{9}$$

Resonant interaction means that the reference frequency $\nu_0$ is contained within the inhomogeneously broadened atomic absorption line and $\mathscr{A}(\vec{r},t)$ is a slowly varying function of time. Atoms are coupled to the field by electric dipole interaction. Because the transition frequency $\nu_{ab}$ is close to $\nu_0$, rapidly oscillating terms can be eliminated from the density matrix equation, which is known as the rotating wave approximation. One is left with the optical Bloch equation

$$\begin{cases}\dot{n}_{ab}=i\left(\Omega\tilde{\rho}_{ba}-\Omega^{*}\tilde{\rho}_{ab}\right)-\gamma_b\left(n_{ab}-1\right)\\ \dot{\tilde{\rho}}_{ab}=-\dfrac{i}{2}\Omega n_{ab}+(i\Delta-\gamma_{ab})\tilde{\rho}_{ab}\end{cases}, \tag{10}$$

where $\Delta=2\pi\left(\nu_{ab}-\nu_0\right)$, $\tilde{\rho}_{ab}=\rho_{ab}e^{-2i\pi\nu_0 t}$ and the Rabi frequency $\Omega$ is defined as $\Omega=\mu_{ab}\mathscr{A}(\vec{r},t)/\hbar$. The Bloch equation can be written in an equivalent integral form as

$$\begin{cases}n_{ab}(t)=1+\left(n_{ab}(t_0)-1\right)e^{-\gamma_b(t-t_0)}+i\int_{t_0}^{t}dt'\left[\Omega(t')\tilde{\rho}_{ba}(t')-\text{c.c.}\right]e^{-\gamma_b(t-t')}\\ \tilde{\rho}_{ab}(t)=\tilde{\rho}_{ab}(t_0)e^{(i\Delta-\gamma_{ab})(t-t_0)}-\dfrac{i}{2}\int_{t_0}^{t}dt'\Omega(t')n_{ab}(t')e^{(i\Delta-\gamma_{ab})(t-t')}\end{cases}. \tag{11}$$

We assume the optical density is sufficiently small so that we can neglect the incoming field attenuation. In the linear response limit $n_{ab}$ is replaced by its initial value $n_{ab}^{(0)} = 1$ in the expression of $\tilde{\rho}_{ab}(t)$ and one obtains

$$\rho_{ab}^{(1)}\left(\nu_{ab}, \vec{r}, t\right) = -\frac{i\mu_{ab}}{2\hbar}\int_0^{\infty} \mathscr{E}_3(\vec{r}, t-\tau)e^{(2i\pi\nu_{ab}-\gamma_{ab})\tau}d\tau\,. \tag{12}$$

Substitution of Eq. (12) into Eq. (6) leads to

$$\tilde{P}(\vec{r},\nu) = \int_{-\infty}^{\infty} P\left(\vec{r},t\right)e^{-2i\pi\nu t}dt = \frac{1}{2}\varepsilon_0\left[\tilde{\chi}^{(+)}(\vec{r},\nu)\tilde{\mathscr{E}_3}(\vec{r},\nu) + \tilde{\chi}^{(-)}(\vec{r},\nu)\tilde{\mathscr{E}_3}(\vec{r},-\nu)^*\right], \tag{13}$$

where

$$\tilde{\chi}^{(\pm)}(\vec{r},\nu) = \mp i\frac{N\mu_{ab}^2}{2\hbar\varepsilon_0}(1-iH)\left[g(\pm\nu)\otimes\mathscr{L}(\pm\nu)\right]. \tag{14}$$

In this expression $\otimes$ stands for the convolution product, $\mathscr{L}(\nu)$ represents the homogeneous line profile,

$$\mathscr{L}(\nu) = \frac{1}{\pi}\frac{\gamma_{ab}/2\pi}{\nu^2 + \left(\gamma_{ab}/2\pi\right)^2}\,, \tag{15}$$

and the Hilbert transform is defined as

$$H\left[f(x)\right] = \frac{1}{\pi}P\int\frac{f(y)}{x-y}dy\,, \tag{16}$$

where *P* denotes a principal value. The atomic response, as given by Eq. (14), reveals two components. One is proportional to the inhomogeneously broadened absorption profile, $g(\pm\nu)\otimes\mathscr{L}(\pm\nu)$. The other component, given by the Hilbert transform of the absorption profile, is the dispersion contribution that expresses causality in the spectral domain. These two components correspond to the response terms $E_R$ and $E_I$ we already met in Section 3.3.2.

Since the transition frequency distribution function $g(\nu)$ only differs from zero in the vicinity of the positive frequency $\nu_0$, $\tilde{\chi}^{(+)}(\vec{r},\nu)$ and $\tilde{\chi}^{(-)}(\vec{r},\nu)$ respectively appear to be positive and negative frequency components of susceptibility, the same as $\tilde{\mathscr{E}_3}(\vec{r},\nu)$ and

$\tilde{\mathscr{E}}_3(\vec{r},-\nu)^*$ are positive and negative frequency components of the field. Therefore the polarization amplitude can be written as

$$\tilde{P}(\vec{r},\nu)=\frac{1}{2}\varepsilon_0\left[\tilde{\chi}^{(-)}(\vec{r},\nu)+\tilde{\chi}^{(+)}(\vec{r},\nu)\right]\left[\tilde{\mathscr{E}}_3(\vec{r},\nu)+\tilde{\mathscr{E}}_3(\vec{r},-\nu)^*\right], \tag{17}$$

such that

$$\tilde{\chi}(\vec{r},\nu)=\tilde{\chi}^{(-)}(\vec{r},\nu)+\tilde{\chi}^{(+)}(\vec{r},\nu)\,. \tag{18}$$

## 4.3. Time-delayed four-wave mixing

The considered architectures all involve a preparation stage where an engraving field $E_e(\vec{r},t)$ spectrum is stored in the atom population difference. Although $E_e(\vec{r},t)$ may result from combination of different beams (typically two beams) with controlled relative phase, the decomposition given in Eq. (8) remains valid. From Eq. (11) one readily obtains the lowest order perturbation to the population difference

$$n_{ab}^{(2)}(\nu_{ab},\vec{r},t)=-\frac{1}{2}\int_{-\infty}^{t}dt'\int_{-\infty}^{t'}dt''\left[\Omega_e(\vec{r},t'')\Omega_e(\vec{r},t')^*e^{i\Delta(t'-t'')}+c.c.\right]e^{-\gamma_{ab}|t'-t''|}e^{-\gamma_b(t-t')}\,. \tag{19}$$

Since the integrant is unchanged under t' and t'' permutation, $n_{ab}^{(2)}(t)$ can be written as

$$\begin{aligned}n_{ab}^{(2)}(\nu_{ab},\vec{r},t)&=-\frac{1}{4}\int_{-\infty}^{t}dt'\int_{-\infty}^{t}dt''\left[\Omega_e(\vec{r},t'')\Omega_e(\vec{r},t')^*e^{i\Delta(t'-t'')}+c.c.\right]e^{-\gamma_{ab}|t'-t''|}e^{-\gamma_b(t-t')}\\&=-\frac{\mu_{ab}^2}{4\hbar^2}\int_{-\infty}^{t}dt'\int_{-\infty}^{t}dt''\left[\mathscr{E}_e(\vec{r},t'')\mathscr{E}_e(\vec{r},t')^*e^{2i\pi\nu_{ab}(t'-t'')}+c.c.\right]e^{-\gamma_{ab}|t'-t''|}e^{-\gamma_b(t-t')}\,.\end{aligned} \tag{20}$$

Let us assume the experiment time scale is much shorter than the upper level lifetime. After the field is switched off $n_{ab}^{(2)}(\nu_{ab},\vec{r})$ reduces to

$$n_{ab}^{(2)}(\nu_{ab},\vec{r})=-\frac{\mu_{ab}^2}{2\hbar^2}S(\vec{r},\nu_{ab})\otimes\mathscr{S}(\nu_{ab})\,. \tag{21}$$

The engraved structure appears to be proportional to the light field power spectrum,

$$S(\vec{r},\nu_{ab})=\left|\tilde{\mathscr{E}}_e(\vec{r},\nu_{ab})\right|^2=\left|\int_{-\infty}^{\infty}\mathscr{E}_e(\vec{r},t)e^{-2i\pi\nu_{ab}t}dt\right|^2, \tag{22}$$

convolved with the homogeneous line profile. Inserting $n_{ab}^{(2)}(\nu_{ab},\vec{r})$ in the expression for the coherence, one readily obtains the engraving field-dependent contribution to the susceptibility

$$\tilde{\chi}^{(\pm)}(\vec{r},\nu)=\pm i\frac{N\mu_{ab}^4}{4\varepsilon_0\hbar^3}(1-iH)\left[g(\pm\nu)S(\vec{r},\pm\nu)\otimes\mathscr{L}(\pm\nu)\otimes\mathscr{L}(\pm\nu)\right]. \qquad (23)$$

If, as is the case in the following, the engraving field $\mathscr{E}_e(\vec{r},t)$ is made up of two components $\mathscr{E}_1(\vec{r},t)$ and $\mathscr{E}_2(\vec{r},t)$, the power spectrum is

$$S(\vec{r},\nu)=\left|\tilde{\mathscr{E}}_1(\vec{r},\nu)\right|^2+\left|\tilde{\mathscr{E}}_2(\vec{r},\nu)\right|^2+\tilde{\mathscr{E}}_1(\vec{r},\nu)^*\tilde{\mathscr{E}}_2(\vec{r},\nu)+c.c.\ , \qquad (24)$$

such that the polarization density contains the term

$$\tilde{P}_{1^*23}^{(+)}(\vec{r},\nu)=i\frac{1}{4}\frac{N\mu_{ab}^4}{\hbar^3}(1-iH)\left[g(\nu)\left(\tilde{\mathscr{E}}_1^*(\vec{r},\nu)\tilde{\mathscr{E}}_2(\vec{r},\nu)\right)\otimes\mathscr{L}(\nu)\otimes\mathscr{L}(\nu)\right]\tilde{\mathscr{E}}_3(\vec{r},\nu). \qquad (25)$$

This expression still differs from the expected product $\tilde{\mathscr{E}}_1^*(\vec{r},\nu)\tilde{\mathscr{E}}_2(\vec{r},\nu)\tilde{\mathscr{E}}_3(\vec{r},\nu)$. The population distribution, as modified by the engraving fields, reflects spectral profiles of those fields provided two conditions are satisfied

i. the initial population distribution $g(\nu)$ should be much broader than $\tilde{\mathscr{E}}_1^*(\vec{r},\nu)\tilde{\mathscr{E}}_2(\vec{r},\nu)$

ii. the spectral resolution, as limited by the homogeneous line profile $\mathscr{L}(\nu)$, should accommodate the fine details of $\tilde{\mathscr{E}}_1^*(\vec{r},\nu)\tilde{\mathscr{E}}_2(\vec{r},\nu)$.

If these conditions are sufficient to make the absorption component in Eq. (25) coincide with $\tilde{\mathscr{E}}_1^*(\vec{r},\nu)\tilde{\mathscr{E}}_2(\vec{r},\nu)\tilde{\mathscr{E}}_3(\vec{r},\nu)$, one is still left with the Hilbert transform distortion that affects the dispersion component spectral selectivity, each atom contributing in inverse proportion to its spectral distance from the probing frequency.

Being in quadrature with the incident field, the dispersion term is washed out in a simple transmission experiment where the probe field co-propagates with the signal and automatically plays the part of a homodyning reference, as seen in Eq. (2) above. In holographic configuration, when the signal does not co-propagate with the probe field, one

must resort to other means in order to restore spectral selectivity. One may heterodyne the signal with a reference that is phase-locked to the probe and demodulate the signal with appropriate phase to reject the dispersion term, as we have seen in Section 3.3.2. Engraving submodulation using a sine wave offers another means to eliminate the dispersive behavior. Let $\tilde{\mathcal{E}}_1^*(\vec{r},\nu)\tilde{\mathcal{E}}_2(\vec{r},\nu)$ be replaced by $\tilde{\mathcal{E}}_1^*(\vec{r},\nu)\tilde{\mathcal{E}}_2(\vec{r},\nu)e^{-2i\pi\nu T}$, where T is adjusted so that $T^{-1}$ is smaller than the characteristic variation scale of $\tilde{\mathcal{E}}_1^*(\vec{r},\nu)\tilde{\mathcal{E}}_2(\vec{r},\nu)$, i.e. smaller than the desired resolution. Then

$$H\left[\tilde{\mathcal{E}}_1^*(\vec{r},\nu)\tilde{\mathcal{E}}_2(\vec{r},\nu)e^{-2i\pi\nu T}\right] \simeq i\tilde{\mathcal{E}}_1^*(\vec{r},\nu)\tilde{\mathcal{E}}_2(\vec{r},\nu)e^{-2i\pi\nu T}, \tag{26}$$

which eliminates the undesired dispersive behavior. One easily generates the spectral submodulation by time delaying the field $\mathcal{E}_2(\vec{r},t)$. Indeed the spectral amplitude of $\mathcal{E}_2(\vec{r},t-T)$ reads as $\tilde{\mathcal{E}}_2(\vec{r},\nu)e^{-2i\pi\nu T}$. Cross-engraving by those time-delayed fields corresponds to the so-called *photon echo configuration* that is now going to be discussed.

## 4.4. Coherent combination of local response: photon echo

By definition, polarization density expresses a local response to excitation by the light fields. Actually Eq. (25) appears to be local both spatially and spectrally. It should be stressed that the sample emission coherently combines the local responses. Response to pulsed excitation represents an important example of such a coherent combination. Let the system be excited by a sequence of two pulses $\mathcal{E}_1(\vec{r},t)$ and $\mathcal{E}_2(\vec{r},t-T)$. According to Eq. (26), provided the characteristic variation scale of $\tilde{\mathcal{E}}_1^*(\vec{r},\nu)\tilde{\mathcal{E}}_2(\vec{r},\nu)$ is much larger than $T^{-1}$ and the homogeneous linewidth, and provided $\tilde{\mathcal{E}}_1^*(\vec{r},\nu)\tilde{\mathcal{E}}_2(\vec{r},\nu)$ is much narrower than $g(\nu)$, the local atomic response is

$$\tilde{P}_{1*23}^{(+)}(\vec{r},\nu) = i\frac{N\mu_{ab}^4}{2\hbar^3}g(\nu_0)\tilde{\mathcal{E}}_1^*(\vec{r},\nu)\tilde{\mathcal{E}}_2(\vec{r},\nu)\tilde{\mathcal{E}}_3(\vec{r},\nu)e^{-2i\pi\nu T-2\gamma_{ab}T}. \tag{27}$$

Contributions from all frequency classes combine into the time domain response

$$P_{1*23}^{(+)}(\vec{r},t)=\int \tilde{P}_{1*23}^{(+)}(\vec{r},\nu)e^{2i\pi\nu t}d\nu = i\frac{N\mu_{ab}^4}{2\hbar^3}g(\nu_0)\mathscr{E}_1^*(\vec{r},-t+T)\otimes\mathscr{E}_2(\vec{r},t-T)\otimes\mathscr{E}_3(\vec{r},t-T)e^{-2\gamma_{ab}T}.$$

This quantity gives rise to the stimulated photon echo signal. The decay factor reflects the atomic coherence relaxation along the signal formation.

# 5. Rainbow analyzer

## 5.1. Principle of operation

The rainbow analyzer concept relies on the engraving of monochromatic gratings in a frequency selective material. Each grating is able to diffract a single spectral component, with a resolution ultimately determined by the homogeneous linewidth of the medium, which is usually less than 1MHz at the temperature of 5K. A large number of gratings can coexist within the inhomogeneous width of the absorption line, which may reach tens of GHz. By varying the laser frequency synchronously with the angle of incidence during the engraving procedure, one associates a specific diffraction angle with each specific spectral component. Therefore, the different spectral components of an incident polychromatic probe beam are diffracted and simultaneously retrieved in different directions. The stack of monochromatic gratings works as a spectrometer which is expected to exhibit a resolution of less than 1MHz and a bandwidth of several tens of GHz. As depicted in Figure 10, radiofrequency spectral analysis can be performed after transfer of the test microwave signal to an optical carrier with the help of a Mach-Zehnder electro-optic modulator (MZM). The bandwidth of the frequency selective medium indeed matches that of integrated MZMs developed for high flow telecommunication. To be more specific, frequency selective media can be devised to cover a bandwidth in excess of 50GHz offered by fast integrated MZMs [64]. Since the spectrometer relies on the angular separation of the frequency components, the number of frequency channels equals the number of different angular directions that can be addressed by the device. For a given setup this number is fixed. However, the engraving laser frequency

scanning range, which determines the spectrometer bandwidth, can be varied easily. By reducing this range while the channel number is kept fixed, one is able to zoom in on a specific spectral region with improved spectral resolution. Since energy is detected in each spectral channel, this processor is independent of the spectral coherence features of the channeled signal, quite in the same way as the spectrum photography architecture presented in Section 3. The potential of a similar arrangement to process the spectral phase and operate as a time-integrating correlator has been addressed in Ref [65]

This rainbow analyzer is reminiscent of the well known acousto-optic spectrometer. In the latter device a Bragg cell achieves two functions. It both transfers the RF signal on the optical carrier and accomplishes the angular separation of the optically carried spectral components. Acoustic wave absorption limits the bandwidth to ~1GHz. The integrated MZM offer a much larger bandwidth. However a MZM transfers only the RF signal on the optical carrier but does not achieve the angular separation of the spectral components, since the carrier and the side bands propagate along the same direction. In the SHB spectrometer, the SHB crystal is intended to complement the MZM component by providing the angular separation.

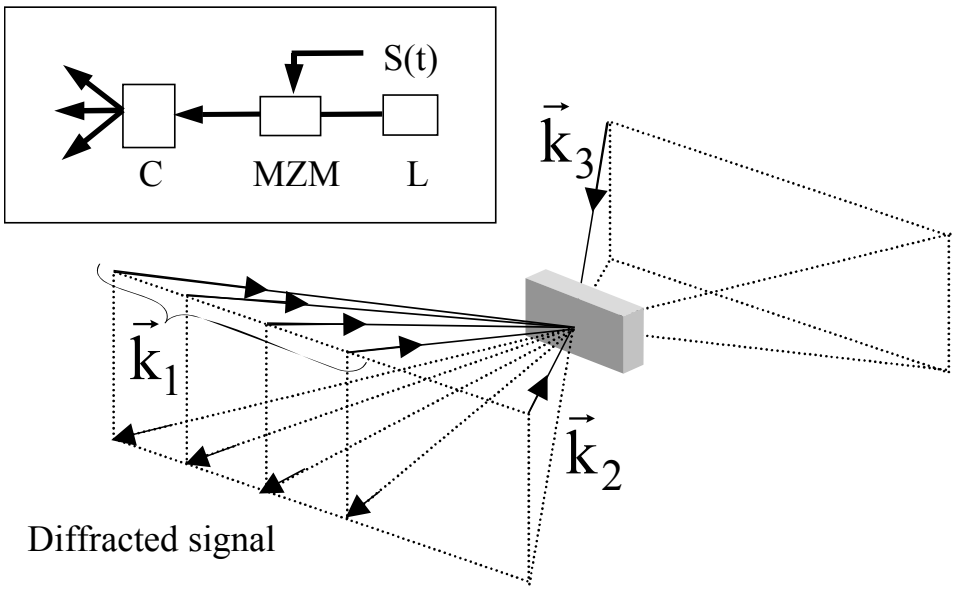

Figure 10. Rainbow spectrometer concept. The insert shows the architecture of the analyzer. A Mach-Zehnder modulator MZM transfers the RF signal S(t) to the optical carrier from laser L. The crystal C diffracts the RF signal frequency components in different directions. The angular separation of the side-band spectral components is effected by the gratings engraved in the SHB crystal. The 3D picture shows the counter propagating box geometry giving independent access to engraving (#1,#2), reading (#3) and diffracted beams.

The beam configuration is strongly constrained by the material limitations. Owing to the short lifetime of the engraving, the gratings must be refreshed continuously and simultaneously diffract the impinging signal beam. This condition is satisfied in the « box configuration » presented in Figure 10. The probe beam that carries the RF signal to be processed propagates along $\vec{k}_3$. It lies out of the plane defined by the engraving beam wave vectors $\vec{k}_1$ and $\vec{k}_2$. This non-coplanar arrangement is consistent with simultaneous writing and readout since the diffracted beam is directed along $\vec{k}_3 + \vec{k}_1 - \vec{k}_2$ which differs from all the incident wave vectors. The wave vectors $\vec{k}_2$ and $\vec{k}_3$ are headed in fixed directions while $\vec{k}_1$ rotates synchronously with the frequency scan of the engraving beams. Therefore the different spectral components that are carried by the probe beam are diffracted in different directions. The « box configuration » satisfies the phase matching condition, $\vec{k}_1 - \vec{k}_2$ being orthogonal to $\vec{k}_3 + \vec{k}_2$.

## 5.2. Programming stage

In the active crystal one engraves the interference pattern of two beams that simultaneously undergo angular and frequency scan. The angular scan is achieved by a frequency-shift compensated pair of acousto-optic deflectors that are crossed successively by beam #1. The deflectors respectively diffract the light beam in order –1 and +1 so that the respective frequency downshift and upshift are subtracted from each other. The two deflectors are oriented in perpendicular directions and are slanted at 45° from the horizontal. When the two deflectors are driven synchronously with a fixed detuning, the emerging beam is scanned horizontally (see Figure 11). An optical relay images the deflectors on the active crystal. This

way, the illuminated spot on the crystal does not move as the beam direction is varied. More specifically, the phase pattern generated at the deflectors is transported to the active medium without distortion.

Let $\vec{k}_{1.0}$ denote beam # 1 wave vector at time t=0. During engraving by fields $E_1$ and $E_2$ the wave vector $\vec{k}_2$ is kept fixed while $\vec{k}_1$ is scanned around the Oy axis, perpendicular to the $(\vec{k}_{1.0}, \vec{k}_2)$ plane, by the AO deflector assembly represented in the insert of Figure 11. The phase shift imparted at position $\vec{\rho}$ in deflector $D_j$ by the acoustic wave obeys the following relation,

$$\Phi_j(\vec{\rho}, t) = \Phi_j(0, t - \frac{\hat{\kappa}_j.\vec{\rho}}{v}), \tag{28}$$

where $\hat{\boldsymbol{\kappa}}_j$ and v respectively represent the sound wave unit vector and the sound velocity. The input phase shift is

$$\Phi_j(0, t) = 2\pi\int_0^t f_j(t')dt', \tag{29}$$

where the linearly chirped acoustic frequency $f_j(t)$ is expressed as

$$f_j(t) = f_j^0 + r_A t, \tag{30}$$

where $f_j^0$ and $r_A$ stand for the AOM central frequency and the chirp rate respectively. The sound wave unit vectors are oriented at 45° from the deflection axis Ox, directed along $\vec{K} = \vec{k}_2 - \vec{k}_1$, and they are orthogonal to each other. The combined phase shift imparted to $E_1$ is

$$\begin{aligned}\Phi(\vec{\rho}, t) &= \Phi_1(\vec{\rho}, t) - \Phi_2(\vec{\rho}, t) \\ &= 2\pi\left[-\frac{x}{v\sqrt{2}}(f_1^0 + f_2^0) - \frac{y}{v\sqrt{2}}(f_1^0 - f_2^0) + (f_1^0 - f_2^0)t - \sqrt{2}\frac{r_A}{v}xt + \frac{r_A}{v^2}xy\right].\end{aligned} \tag{31}$$

The first two terms on the right hand side respectively represent the horizontal and vertical deflection at time t=0. Despite of the chirp they undergo, the acoustic waves convey a fixed

optical frequency shift $f_1^0 - f_2^0$ to the light beam. This is reflected in the third term. The fourth term in Eq. (31) corresponds to the time dependent angular deflection. The last term is a time-independent, purely spatial quadratic phase. In other words a chirped acousto-optic deflector behaves as a lens, the focal length of which depends on the chirp rate. An AO deflector would mimic a cylindrical lens since it operates along a single direction. In our setup this quadratic phase factor modifies imaging conditions and degrades the spectral resolution.

The first two terms in the phase expression (Eq. (31)) are incorporated in the wave vector $\vec{k}_{1.0}$ at t=0. The laser frequency is swept at rate r synchronously with the angular scan. Then the complex fields are

$$\begin{aligned} \mathcal{E}_1(\vec{\rho},t) &= \mathcal{E}_0(\vec{\rho})e^{2i\pi\left(\nu_1 t+\frac{1}{2}rt^2\right)-2i\pi\sqrt{2}\frac{r_A}{v}xt+2i\pi\frac{r_A}{v^2}xy}, \\ \mathcal{E}_2(\vec{\rho},t) &= \mathcal{E}_0(\vec{\rho})e^{2i\pi\left(\nu_2 t+\frac{1}{2}rt^2\right)-i\vec{K}.\vec{\rho}}, \end{aligned} \tag{32}$$

where the gaussian beam Rabi frequency spatial distribution is expressed in terms of the beam waist at the AOD, $w_{AO}$, as

$$\mathcal{E}_0(\vec{\rho}) = \mathcal{E}_0(0)\exp\left(-\frac{\rho^2}{w_{AO}^2}\right) \tag{33}$$

and where $\nu_1 = \nu_2 + f_1^0 - f_2^0$. The AOD is imaged on the active crystal with magnification factors $m_x$ and $m_y$ along directions x and y respectively. As recalled in section 4, low intensity engraving can be described in terms of the incident light power spectrum $\left|\tilde{\mathcal{E}}_1(\vec{\rho},\nu)+\tilde{\mathcal{E}}_2(\vec{\rho},\nu)\right|^2$. The cross-term $\tilde{\mathcal{E}}_1^*(\vec{\rho},\nu)\tilde{\mathcal{E}}_2(\vec{\rho},\nu) = \frac{1}{r}\mathcal{E}_0^2(\vec{\rho})e^{i\Psi(\vec{\rho},\nu)-2i\pi\frac{r_A}{v^2}xy-i\vec{K}.\vec{\rho}}$, where

$$\Psi(\vec{\rho},\nu) = \frac{\pi}{r}\left(\nu-\nu_1+\frac{x}{v}r_A\sqrt{2}\right)^2-\frac{\pi}{r}\left(\nu-\nu_2\right)^2, \tag{34}$$

as derived from the Fourier transform of Eq. (32), gives rise to the diffraction gratings dedicated to the spectral analysis of the optically carried RF signal. The phase $\Psi(\vec{\rho},\nu)$ can be rearranged as

$$\Psi(\vec{\rho},\nu) = -2\pi(\nu-\nu_1)T + 2\pi\frac{r_A^2}{rv^2}x^2 + 2\pi\frac{r_A\sqrt{2}}{rv}(\nu-\nu_1)x - \pi rT^2, \qquad (35)$$

where $T = \left(f_1^0 - f_2^0\right)/r$. The acoustic wave detuning that appears in Eq. (32) leads to a fixed frequency shift of the deflected beam with respect to the fixed direction engraving beam. Since the laser is frequency chirped, each ion interacts with the two beams at successive moments separated by delay T. As discussed in Ref. [66] and recalled in sections 4.3 and 4.4, the interaction delay makes the setup operate in a photon echo configuration and results in submodulation of the level population difference spectral distribution, which should optimize the spectral resolution and the signal diffraction efficiency. However, in contrast to conventional photon echo experiments in which all atoms at a specific transition frequency undergo the same excitation independent of their location, in the present case, atoms at different spatial positions are excited in a different way. As a result, the photon echo behavior is not visible at the local level, i.e. before summing over both the spatial and frequency distribution of the atoms. The spectral behavior of the crystal response results from the coherent combination of local emissions all over the illuminated spot.

## 5.3. Spectral resolution

Let a monochromatic Gaussian probe beam at frequency $\nu$ be directed to the sample along $\vec{k}_3$. The probe beam is assumed to exhibit the same spatial distribution $\mathcal{E}_0(\vec{\rho})$ as the engraving beams. The linear response of the engraved diffraction grating at the image of position $\vec{\rho}$ is given by Eq. (25). The local radiated field, proportional to this response, can be expressed as

$$\tilde{\mathscr{E}}(\vec{\rho},\nu) \propto \tilde{\mathscr{A}}(\vec{\rho},\nu) e^{-i\left(k_3+\vec{K}\right).\vec{\rho}}, \tag{36}$$

where

$$\tilde{\mathscr{A}}(\vec{\rho},\nu) \propto \left(1-iH\right)\left[\mathscr{E}_0^3(\vec{\rho}) e^{-i\Psi(\vec{\rho},\nu)-2i\pi\frac{r_A}{v^2}xy} \otimes \mathscr{S}(\nu) \otimes \mathscr{S}(\nu)\right]. \tag{37}$$

In the frame of the Huygens-Fresnel principle Fraunhofer approximation, the signal emitted at angular distance $(\varphi,\theta)$ from direction $\vec{k}_3+\vec{K}$ combines the local contributions through the following Fourier transform of $\tilde{\mathscr{A}}(\vec{\rho},\nu)$ ,

$$\underline{\tilde{\mathscr{A}}}(\varphi,\theta,\nu) = \int dX \int dY \tilde{\mathscr{A}}(\vec{\rho},\nu) e^{\frac{2i\pi}{\lambda}(\varphi X+\theta Y)}, \tag{38}$$

where space coordinates X and Y are now expressed at the crystal. Performing the space integration first, one finds

$$S(\nu,\varphi,\theta) = \left|\underline{\tilde{\mathscr{A}}}(\varphi,\theta,\nu)\right|^2 = \left|\left(1-iH\right)\left[\left(e^{-2i\pi(\nu-\nu_1)T} g(\nu-\nu_1,\varphi,\theta)\right) \otimes \mathscr{S}(\nu-\nu_1) \otimes \mathscr{S}(\nu-\nu_1)\right]\right|^2 \tag{39}$$

where

$$g(\nu,\varphi,\theta) = e^{-2Ln2\left\{\left[\left(\nu\frac{\bar{\varphi}}{\bar{\nu}}+\varphi\right)/\delta\varphi\right]^2+\left[\theta/\delta\theta\right]^2\right\}}, \tag{40}$$

$$\delta\varphi = \frac{\sqrt{6Ln2}}{\pi}\frac{\lambda}{m_x w_{AO}}\sqrt{1+\alpha^2}\ ,\ \delta\theta = \frac{\sqrt{6Ln2}}{\pi}\frac{\lambda}{m_y w_{AO}}\sqrt{1+\alpha^2}\ , \tag{41}$$

$$\alpha = \frac{\pi}{2}\frac{r_A w_{AO}^2}{v^2}, \tag{42}$$

and $\bar{\nu}$ represents the frequency interval over which the laser is scanned while $\varphi$ is varied over the angular range $\bar{\varphi}$. If the submodulation period 1/T is much smaller than the width $\bar{\nu}\delta\varphi/\bar{\varphi}$ of $g(\nu,\varphi,\theta)$, the signal intensity reduces to

$$S(\nu,\varphi,\theta) = e^{-4t_{12}/T_2}\left|g(\nu-\nu_1,\varphi,\theta)\right|^2. \tag{43}$$

This is the well known photon echo situation that leads to optimal spectral resolution by eliminating the dispersive part of the diffracted signal [67]. According to Eq. (43) the spectral component $\nu_1$ is diffracted in direction $(\varphi = 0, \theta = 0)$. The angular full width at half maximum of the diffracted beam is given by $(\delta\varphi, \delta\theta)$. The spectral component $\nu$ is diffracted in direction $(\varphi_\nu = (\nu - \nu_1)\overline{\varphi}/\overline{\nu}, \theta = 0)$, with the same angular spreading as component $\nu_1$. The angular spreading of each frequency channel limits the spectral resolution of the spectrum analyzer to $\delta\nu = \overline{\nu}\dfrac{\delta\varphi}{\overline{\varphi}} = \overline{\nu}\dfrac{v}{w_{AO}\overline{f}}\dfrac{\sqrt{6Ln2}}{\pi}\sqrt{1+\alpha^2}$, where $\overline{f}$ stands for the acoustic frequency scanning range of the AOD. The frequency resolution is independent of the optics magnification factor. It depends only on the engraving laser scanning range and on the number of directions that can be addressed by the AOD. The photon echo configuration also limits the effects of bleaching by the probe, as discussed in ref [68].

The parameter $\alpha$ characterizes the AOD lens effect. On account of the AOD driver frequency chirp, the two sides of the laser spot undergo deflection at different angles in the AOD. The angle difference can be expressed in terms of the chirp rate and of the acoustic wave transit time across the light beam, $w_{AO}/v$, as $\lambda r_A w_{AO}/v^2$. This angle has to be compared with the divergence of the laser beam, $\lambda / w_{AO}$. The parameter $\alpha$ is nothing but the ratio of these two quantities. The lensing effect is negligible when $\lambda r_A w_{AO}/v^2 << \lambda / w_{AO}$. The channel broadening caused by the acousto-optic deflector pair lens effect is not a fundamental limitation. On account of the holographic storage properties, the corresponding wave front distortion does not entail irreversible signal alteration. The quadratic cross phase factor can be alleviated by an appropriate non-axially symmetric wave front correction to any of the four fields involved in the signal formation.

The last piece of information we derive from Eq (39) is the signal intensity variation as a function of the two engraving beam detuning. Integrating Eq. (39) one obtains

$$S(\nu,\varphi_\nu,0)=\left[1+\mathrm{erf}(u)\right]^2 e^{-4t_{12}/T_2}, \tag{44}$$

where $u=\dfrac{\pi\bar{\nu}t_{12}\delta\varphi}{\bar{\varphi}\sqrt{2\mathrm{Ln}2}}-\dfrac{\bar{\varphi}\sqrt{2\mathrm{Ln}2}}{\pi\bar{\nu}T_2\delta\varphi}$.

## 5.4. Experimental setup

We have investigated various aspects of the rainbow analyzer, such as bandwidth flexibility [66][69] and dynamic range [66]. The largest channel number was obtained with the setup we describe here. The programming beam #1 goes through a 2D deflector device (A&A DTS XY 250) that offers 5 mm clear aperture, and 69 mrad scanning range as the common driving frequency is varied from 85MHz to 125MHz. An optical relay, with a magnification factor $m_x$ =0.25, images the deflector on the SHB crystal so that the illuminated spot does not move as the beam direction is varied. The two output channels of a 1Gigasample/s arbitrary wave form generator (Sony/Tektronix AWG520) separately drive the two AOs that are combined in the deflector. This enables us to set a fixed frequency detuning between the two chirped synchronized driving waves.

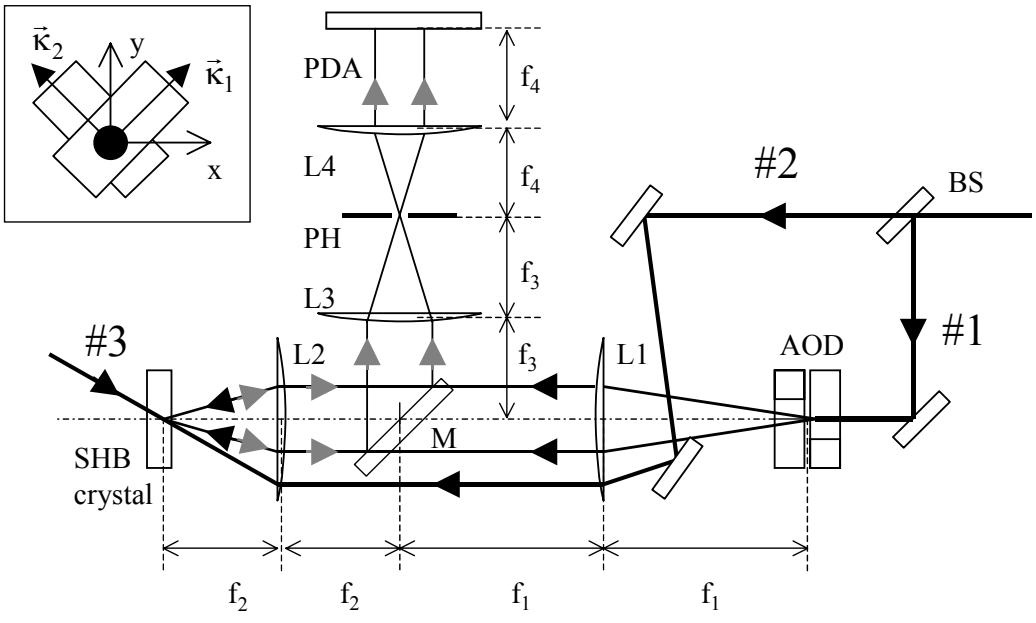

Figure 11. 100-channel set-up. After the beam splitter BS the beam #1 is directed to the acousto-optic deflector AOD. Through the lenses L1 and L2, the fixed beam #2 and the scanned beam #1 are made to overlap in the SHB crystal. The RF signal carrier beam #3 is diffracted on the engraved gratings. The diffracted beams counter propagate beneath the light sheet formed by beam #1. The non-coplanar arrangement is not visible in this top view of the set up. Through the lens L2, the mirror M and the lens L3 the diffracted beams converge to the pin-hole PH, placed in imaging position with respect to the crystal. Finally they reach the photodiode array PDA that is positioned in the Fourier plane of PH through the lens L4. The focal distance of lens $L_i$ is denoted by $f_i$. $f_2/f_1=0.25$, $f_3/f_2=0.5$, $f_4=150$mm. The AO deflector assembly is shown in the insert. The acoustic wave vectors are denoted by $\vec{\kappa}_1$ and $\vec{\kappa}_2$.

The synchronized laser frequency chirp and beam angular scan must be repeated over the spectrometer bandwidth with precision better than the desired resolution, since the grating storage is accumulated in the active crystal for several engraving cycles. To satisfy the repeatability requirements of our application it was necessary to develop a novel electro-optically-tuned extended-cavity diode-laser [70], [58]. The laser we use in this experiment, equipped with an improved AR coated chip, is easily scanned without mode hopping over a 3.5GHz interval. In more recent experiments demonstrating the spectrum photography architecture we have been able to increase the scanning range to 10GHz (see Section 3).

In previously studied photon echo applications, accumulation is regarded as a demanding procedure [71], [72]. In these applications the storage coordinate is the time delay of the engraving fields. The delay dependent phase shift that is stored in the material is increasingly affected by laser frequency fluctuations as one increases the delay range. A 1μs delay storage range requires at least 100kHz laser stability during a 10 ms long accumulation process [72]. The present situation is somewhat different. All the gratings associated with the different spectral channels are engraved with the same delay that only has to be larger than the inverse spectral resolution. For 33MHz resolution, this delay need not exceed ~10ns, which is much smaller than the inverse jitter range of a free running extended cavity diode laser over a 10 ms time interval.

Since we split the three needed beams from a single laser, we have to operate in a sequenced mode, where grating engraving and signal diffraction alternate. Engraving takes place during the first half repetition period, while the laser frequency is kept fixed for readout

during the second half period. With a repetition rate of 2kHz, the 250µs-long writing step is followed by a same duration step devoted to RF signal spectral analysis. Since the shelving state lifetime is ~10 ms, engraving is accumulated over ~20 writing steps.

The modulated probe beam to be spectrally analyzed is directed to the $Tm^{3+}$: YAG crystal and is diffracted on the engraved gratings into a frequency-dependent direction (see Figure 11). In order to filter out the stray light scattered off the cryostat windows, we make the diffracted beams converge to a pin hole with the help of the optical relay formed by the lenses $L_2$ and $L_3$. The pin hole is sized to the dimensions of the active area image formed through lenses $L_2$ and $L_3$. Emerging from this precisely defined emitting area, the diffracted beams are collected on a photodiode array (PDA) through the lens $L_4$ operating as an angle-to-position Fourier transformer. The PDA includes 1024 pixels. The pixels are 2.5 mm high and 25 µm wide. They are sequentially read out every 10 ms. Since the detector is operating continuously, this interval also represents the integration time.

The illuminated position coordinate on the PDA is proportional to the diffraction angle and so to the RF signal frequency. Specifically, a beam diffracted in direction $\varphi$ strikes the PDA at position $x - x_0 = (\varphi - \varphi_0) f_4 f_2 / f_3$, where the focal length of lens $L_i$ is denoted by $f_i$. The direction $\varphi$ is connected to the RF frequency by $\varphi - \varphi_0 = \bar{\varphi}(\nu - \nu_0)/\bar{\nu}$ where $\bar{\varphi}$ and $\bar{\nu}$ respectively represent the angular scanning range of beam #2 and the frequency chirp range of the laser during the engraving step. The spectral channel number of the device is given by the number of different directions that can be addressed by the AO deflector.

## 5.5. Experimental results

Using this setup we demonstrate a 3.3GHz instantaneous bandwidth with 100-channel resolution. Experiments have been performed with a 2.5mm-thick, $Tm^{3+}$:YAG (0.5 at. %) crystal. We simulate a multiple-line RF signal by making the laser perform various discrete frequency jumps during the readout step of the writing/readout sequence. The staircase

frequency scan of the probe beam is illustrated in Figure 12. The laser stays for 10μs at each frequency step. In a previous publication [69] we demonstrated the spectral analysis of a RF signal that was put on the probe beam with the help of a Mach-Zehnder modulator.

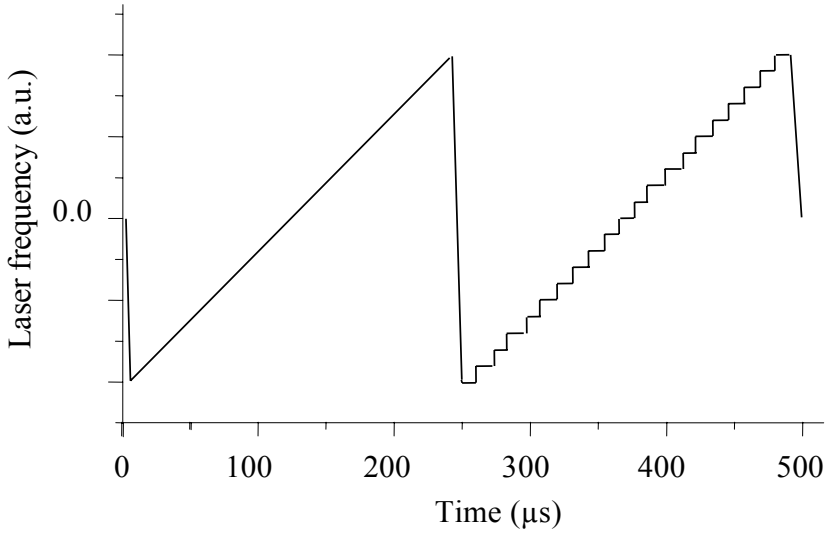


Figure 12. Time diagram of the laser frequency scan. During the first 250μs the laser is continuously scanned over the selected bandwidth as it engraves the spectrally selective holograms. During the second half of the sequence, a multiple-line spectrum is simulated by a stair case frequency scan. The laser stays for 10μs at each step.

In order to increase the intensity, we have reduced the vertical spot size to 150μm. With a beam waist at the deflector $w_{AO}$= 1.5mm, and a magnification factor $m_x = 0.25$, the horizontal spot size is 750μm. The fixed engraving, deflected engraving, and probe beam powers are amount to 4.7mW, 3.2mW and 0.7mW, respectively. An experimental spectrum is displayed in Figure 13.

Given the acoustic wave velocity v= 650m/s, the acoustic wave chirp rate $r_A = 1.2\ 10^{11} s^{-1}$, Eq. (41) predicts an angular resolution $\delta\varphi = 1.64$mrad, which corresponds to ~5 pixels of the PDA. We actually measure an angular resolution of ~6 pixels. Combined with a 205mrad scanning range, this resolution offers a 100-channel capacity. The angular scanning range is accidentally limited to 205mrad because of a beam folding mirror size. The XY AO deflector (AOD) actually offers more than 270 mrad scanning range, which corresponds to 135

channels. Compensation of the acousto-optic lens effect mentioned in section 5.3 would probably increase this number by reducing the channel width.

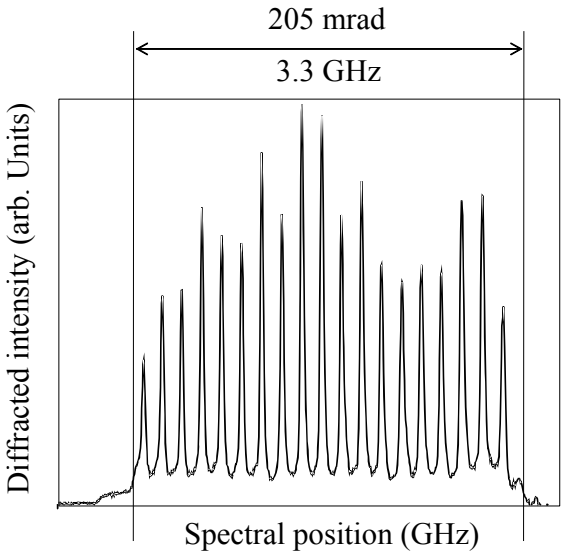


Figure 13. RF spectral analyzer demonstration. The simulated multi-frequency RF signal undergoes 19 successive 175MHz-wide jumps, and dwells only 10μs at each spectral position. This demonstrates 3.3GHz instantaneous bandwidth and 100-channel capacity.

## 5.6. Future Improvements

In order to continuously detect the optically carried RF signal, without dead time, one has to refresh the engraved gratings and to analyze the signal simultaneously. The single laser we used in the reported experiment was not able to accomplish these two tasks. Two different lasers are needed since the engraving beam frequency has to be continuously scanned at fixed rate, while the RF signal to be investigated must be transferred onto a fixed frequency carrier. The relative stability of the two lasers should be better than the expected resolution of the spectrum analyzer. In order to proceed toward 100% duty cycle operation, we demonstrated an active stabilization scheme where the laser frequencies are periodically compared after each frequency scan of the engraving laser [73].

The number of resolved spectral channels is closely related to the time×bandwidth product of the AOD. Indeed this product represents the number of different directions that can be addressed by the AOD. Used with a Gaussian beam expanded to the maximum held

diameter of 4.2mm at $1/e^2$, and operated over a 40MHz acoustic wave bandwidth, the A&A DTS XY 250 deflector offers a time×bandwidth product of ~350. A larger device with a clear aperture of ~14mm would be needed to reach a 1000 channel resolution. Such a wide aperture probably excludes the use of an XY AO device. The frequency shift caused by a single dimension deflector could be compensated easily with an AO shifter placed on the other engraving beam.

As for the dynamic range, our best 35dB result [66] could be improved by reduction of stray light. The cryostat windows probably contribute significantly to this undesired background. Their number should be reduced. This demands that most optics be enclosed within an evacuated box, the active crystal itself being attached to a cold finger inside this box.

## 6. Photon echo chirp transform spectrum analyzer

As the rainbow analyzer, the photon echo chirp transform analyzer uses the crystal as a processor. Whereas the rainbow analyzer makes the crystal a frequency-to-angle converter, the chirp transform analyzer uses the crystal as a frequency-to-time converter. No spatial dimension is used in this architecture. Instead one uses the photon echo process to produce the Fourier transform of the RF carrying beam, thus producing a temporal image of the RF spectrum. This transformation relies on the coherent combination of the emissions from the ions with resonant frequencies distributed over a wide domain, typically equal to the crystal inhomogeneous width. This must be contrasted with the rainbow or the photographic plate analyzers that require no phase relation between the atomic coherences carried by ions with different transition frequencies.

## 6.1. Photon echo chirp transform

### 6.1.1. Chirp transform and photon echoes

The chirp transform algorithm [41] computes the Fourier transform $\tilde{s}(\nu)$ of a signal $s(t)$ according to

$$\tilde{s}(\nu = rt) = \left[ \left( s(t)\, \mathrm{e}^{-i\pi r t^2} \right) \otimes \mathrm{e}^{i\pi r t^2} \right] \mathrm{e}^{i\pi r t^2} . \tag{45}$$

This process is also called the MCM scheme since it involves a multiplication followed by a convolution and a last multiplication. The last multiplication simply corrects for a phase factor and can be dropped when only the modulus of the Fourier transform is of interest. We then have the MC scheme. In paraxial diffraction theory, the MC process is the one that yields, in the focal plane of a lens, the space frequency spectrum of an object situated just before the lens. The object is first multiplied by the transmission factor of the lens. Diffraction to the focal plane makes the convolution.

In the time domain (Eq.(45)), the phase quadratic factor represents a linear frequency chirp with chirp rate $r$. The multiplication means modulating a chirp by the signal $s(t)$, or equivalently performing quadratic phase modulation of the signal. This multiplication is the operation of a so-called time lens [74],[75] whose focal time is $\nu_0 / r$ with $\nu_0$ the optical frequency. The convolution assigns different delays to the different input frequencies, with a linear relation of coefficient $1/r$ between delay and frequency. It is a dispersion process of dispersion rate $1/r$.

The aperture of the time lens - the maximum duration of the signal that can be quadratically phase modulated - sets the spectral resolution of the chirp transform. The maximum signal bandwidth that can pass through the lens sets both the lens and the process bandwidth. However, the dispersive delay line features must be taken into account. Not only must its dispersion rate match the lens focal time, but its bandwidth must also exceed that of

the lens, and its maximum delay - the delay between the two extreme frequencies of the bandwidth - must be greater than the lens aperture.

The chirp transform algorithm has already been implemented for RF spectral analysis purposes with acousto-optic and surface acoustic wave (SAW) devices [76]. The latter are the sole commercial devices. They perform a maximum bandwidth of 500 MHz, an ultimate resolution down to 10 kHz, and a time bandwidth product up to 2500 [77]. Although impressive, these devices cannot cope with multi GHz bandwidth. Optical solutions may overcome this limitation.

Photon echoes in rare earth doped crystals are potentially a good solution. The optoelectronic architecture we propose is sketched in Figure 14. A cw laser with chirping capability, the so-called frequency agile laser source, produces a microsecond long optical chirp spanning a multi GHz bandwidth [70]. This optical carrier is then modulated by the RF signal in an integrated Mach Zehnder electro optic modulator (MZM). This makes the multiplication, i.e., our time lens effect. The beam is then directed toward a dispersive delay line engraved in a rare earth doped crystal by another frequency agile laser. The output of the crystal is detected on a fast photodiode which directly yields the rf spectrum. Thanks to the matching features of frequency agile lasers, rare earth doped crystals, fast MZM and photodiodes, development of a multi GHz bandwidth spectral analyzer with resolution below 1 MHz, and great flexibility, should be possible.

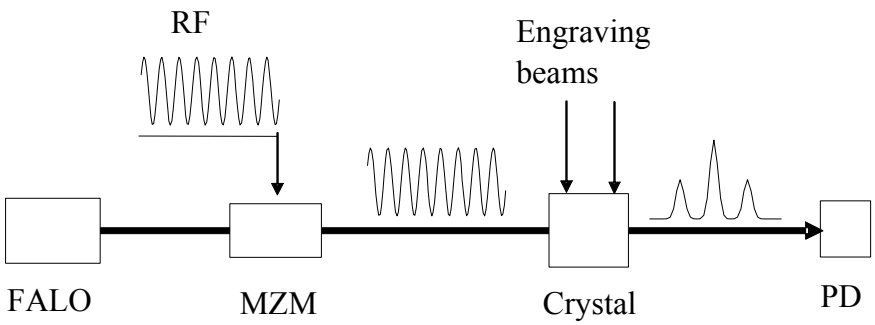


Figure 14. Architecture of the photon echo chirp transform RF spectrum analyzer. FALO: frequency agile laser oscillator, MZM: Mach Zehnder modulator, PD: photodiode.

As demonstrated in section 4.4, in the perturbation regime the stimulated photon echo signal $\mathscr{E}_e(t)$ is described by

$$\begin{aligned} \mathscr{E}_e(t) &= \mathscr{E}_1^*(-t) \otimes \mathscr{E}_2(t) \otimes \mathscr{E}_3(t) \\ \tilde{\mathscr{E}}_e(\nu) &= \tilde{\mathscr{E}}_1^*(\nu) \tilde{\mathscr{E}}_2(\nu) \tilde{\mathscr{E}}_3(\nu) \end{aligned} , \tag{46}$$

where $\mathscr{E}_i(t)$ and $\tilde{\mathscr{E}}_i(\nu)$ are the complex amplitudes of the three excitation pulses and their Fourier transforms. The first two pulses engrave the frequency domain interference pattern $\tilde{\mathscr{E}}_1^*(\nu)\tilde{\mathscr{E}}_2(\nu)$ in the absorption band of the material. This engraving is a coherent filter which lasts for the lifetime $T_1$ of the upper level of the transition. The third pulse, usually called the reading or probing pulse, is spectrally filtered by this coherent filter to yield the echo signal. As explained in section 4.4, Eqs. (46) implicitly suppose that the engraved filter contains a sinusoidal submodulation of period smaller than the field spectral amplitudes so as to remove the dispersive component of the filter response. The bandwidth of the process is limited by that of the material, which is given by the inhomogeneous width $\Gamma_{inh}$ of the optical transition. The spectral resolution is limited by the homogeneous linewidth $1/\pi T_2$ of the transition, where $T_2$ is the optical transition coherence time.

Expression (46) can be arranged such that the echo signal gives the spectrum of the RF signal $s(t)$ according to the MC scheme. Let the first two pulses be such that their correlation is the quadratic phase factor $\exp(i\pi r t^2)$. This is the case, for instance, if the first pulse is a short pulse represented by the Dirac distribution $\delta(t)$ and the second pulse the optical chirp $\exp(i\pi r t^2)$. Now let the third pulse be an optical chirp $\exp(-i\pi r t^2)$ modulated by an RF signal $s(t)$. The echo signal becomes

$$E_e(t) = \tilde{s}(rt)\exp(i\pi r t^2) . \tag{47}$$

The echo signal time evolution therefore gives the Fourier transform of the RF signal $s(t)$, carried by an optical chirp. Photo-detection of the echo power directly yields the power spectrum $\left|\tilde{s}(rt)^2\right|$.

6.1.2. A physical picture

The process is conveniently represented in the time and frequency plane. Let us first consider the configuration of Figure 15. It represents the three exciting pulses and the echo signal in the time and frequency plane. The first pulse is a short pulse whose bandwidth spans an interval $\Delta$. The second pulse is an optical chirp of duration $\tau_2 - \tau_1$ which spans the same $\Delta$ bandwidth. For the excited ions, the delay between the first and second excitations is a linear function of the ion resonant frequency. More precisely, as one easily deduces from Figure 15, that the delay is

$$\begin{aligned} \tau(\nu) &= \tau_1 + (\nu - \nu_1)/r \\ r &= \Delta/(\tau_2 - \tau_1) \end{aligned}, \tag{48}$$

where $\nu_1$ (resp. $\nu_2$) is the frequency corresponding to delay $\tau_1$ (resp. $\tau_2$) and the parameter $r$ is the chirp rate of the second pulse. The ions excited by the two pulses record the delay between the two excitations. Since this delay is a linear function of frequency, one actually records a dispersive filter. Recording is physically represented by a chirped sinusoidal modulation of the crystal inhomogeneous absorption band. The dispersion rate $\mathrm{d}\tau/\mathrm{d}\nu$ is the inverse $1/r$ of the chirp rate.

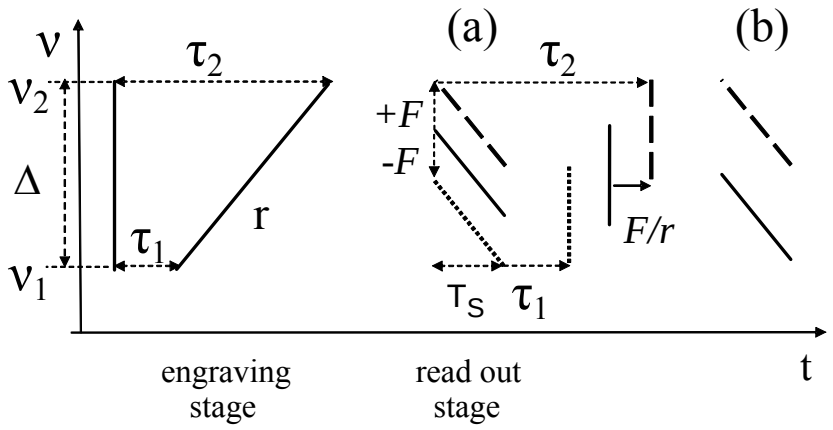


Figure 15. Representation of the photon echo chirp transform process in the time-frequency plane. The first excitation is provided by a short pulse of bandwidth $\Delta$ drawn as a line parallel to the frequency axis. The next slanted line of slope $r$ represents the chirp which makes the second excitation. The third slanted continuous line is the laser reading chirp with rate $-r$, and duration $T_s$. It generates the echo peak represented as a continuous vertical line. The dotted (resp. dashed) line parallel to the laser reading chirp line is the lower (resp. upper) side chirp due to modulation by the RF signal of frequency $F$. It generates the echo peak in dotted line (resp. dashed). (a) represents the reading chirp configuration for double sideband RF spectral analysis, while (b) represents the reading chirp for single sideband analysis. In (b) the continuous line is the laser reading chirp while the dashed line is the upper RF sideband chirp.

The third pulse is an optical chirp of rate $-r$ and duration $T_s$ modulated by an RF signal. Let us first consider the chirped optical carrier. It excites the ions of frequency $\nu$ at time $t_3 = t_3(\nu_2) - (\nu - \nu_2)/r$. The different ions then emit an echo signal which is delayed with respect to excitation time by the very delay $\tau(\nu)$ the ions have recorded between the first two excitations. Therefore the echo generated by ions of frequency $\nu$ appears at time $t_e(\nu) = t_3(\nu) + \tau(\nu) = t_3(\nu_1) + \tau_1$. Consequently, all the elementary echoes generated by the ions of different frequencies actually appear at the same time. Their coherent addition gives an echo whose duration is naturally given by the inverse of the bandwidth $rT_s$ which participates to signal formation.

Now let us consider RF modulation. Modulating an optical chirp by an RF signal of frequency $F$ generates two symmetric side chirps shifted by $\pm F$ from the optical carrier. This RF modulated chirp will therefore generate three echo peaks. One for the carrier as discussed above and one for each side chirp, time delayed by $\pm F/r$ with respect to the

optical-carrier echo peak. Hence the echo signal displays the RF signal spectrum with the time-to-frequency correspondence $F = (t - t_0)/r$ where $t_0$ corresponds to the optical-carrier echo peak. One notices on Figure 15 that the three echo peaks appear centered at different frequencies. This results from direct graphical construction of these echo peaks. It means that the echo peaks are on a chirped carrier. The chirp rate is easily computed to be $r$ from Figure 15, which is in agreement with Eq. (47).

6.1.3. Expected features

The features of this photon echo MC scheme, regarding its application to spectral analysis of RF signals, can easily be deduced from the graphical representation given above. The bandwidth $\Delta$ and the maximum delay $\tau_2$ of the dispersive filter engraved in the crystal are limited, respectively, by the inhomogeneous width $\Gamma_{inh}$ and the coherence time $T_2$ of the transition. Some conditions must be imposed to the RF signal. First, one requires that the total bandwidth occupied by the reading chirp, with its RF sidebands, be less than $\Delta$. This implies that

$$2\Delta_s + rT_s \leq \Delta\,, \tag{49}$$

with $rT_s$ the reading chirp bandwidth and $\Delta_s$ the signal bandwidth. This necessitates that the spectral domain swept by the reading chirp be in the center of the spectral domain occupied by the dispersive filter.

One also requires that the whole echo signal appears after the end of the reading chirp. This is a strict condition for the echo to give the Fourier transform of the RF signal. This time separation condition is

$$\tau_1 \geq 0\,, \tag{50}$$

as deduced from Figure 15.

We also want to be able to perform continuous spectral analysis of an incoming RF signal. For that purpose, one must generate a continuous succession of identical reading chirps, with ideally zero delay between two successive chirps. Then each reading chirp generates an echo which gives the spectrum of the RF signal carried by the chirp. Real time spectral analysis is performed with 100% probability of interception. The echo from one chirp arises during the next reading chirp. Angular separation of the echo from the reading chirp allows such timing. However one must ensure that the successive echoes do not overlap in time. In other words, the duration of the echo generated by one reading chirp must be less than the chirp duration

$$2\Delta_s / r \le T_s \ . \tag{51}$$

In order to fully exploit the capabilities of the dispersive filter, one considers Eqs (49) and (50) as equalities. We therefore end up with the conditions

$$\begin{aligned} &\Delta_s = \tfrac{1}{2}\Delta(1 - T_s / \tau_2) \ , \\ &\tau_1 = 0 \ , \\ &T_s \ge \tau_2 / 2 \ . \end{aligned} \tag{52}$$

The maximum time bandwidth $\Delta_s T_s$ product of the analyzer is obtained for $\Delta_s = \Delta / 4$ and $T_s = \tau_2 / 2$. For greater bandwidth, that is shorter $T_s$, the condition for continuous analysis cannot be respected and the probability of interception is less than 100 %.

6.1.4. Single side band analysis

For spectrum analysis purpose, one need only see a single RF sideband. The reading chirp configuration of Figure 15b achieves spectrum analysis of the upper RF sideband. For that purpose the lower frequency of the spectral domain swept by the reading chirp is set to coincide with the lower frequency of the spectral filter. Consequently, the lower RF sideband chirp falls partly out of the dispersive filter domain. But we are interested only in the upper RF sideband, and condition (49) now becomes $rT_s + \Delta_s \le \Delta$. We also set $\tau_1 = 0$. This ensures

that the echo signal corresponding to the upper sideband appears only after the end of the reading chirp. The signal generated by the lower sideband appears during the chirp. The condition for continuous analysis is unchanged. We therefore end up with the following conditions:

$$\begin{aligned} &\Delta_s = \Delta(1 - T_s / \tau_2) \ ; \\ &\tau_1 = 0 \ ; \qquad\qquad . \\ &T_s \geq \tfrac{2}{3}\tau_2 \ . \end{aligned} \tag{53}$$

The maximum time bandwidth product is obtained for $\Delta_s = \Delta/2$ and $T_s = \tau_2/2$ and is $1/4$ of the available product $\Delta T_2$ in the crystal. However these values do not satisfy the condition for continuous analysis. At the limit of this condition, one has $T_s = 2\tau_2/3$ and $\Delta_s = \Delta/3$. Let us note that the continuous analysis condition can be somewhat relaxed depending on the application.

6.1.5. Influence of the material finite coherence time

As noted above the finite coherence time $T_2$ of the optical transition limits the maximum delay of the dispersive line. Hence it limits the maximum duration $T_S$ of the reading chirp, and therefore the spectral resolution $1/T_s$ of the spectrum analyzer.

The coherence time also affects the signal amplitude. As can be observed from Figure 15, the spectral domains contributing to the formation of the different echo peaks are different. Different spectral domains also mean different delay ranges in the dispersive filter. Thus, higher RF frequencies probe longer delays in the dispersive filter. From simple graphical construction one expects to see an $\exp(-4t/T_2)$ time dependence of the echo signal power.

In order to investigate this feature, we compute the expected signal accounting for finite coherence time. Assuming a low intensity reading chirp with constant amplitude over its duration $T_s$, one gets the expression

$$\left|E_e(t)^2\right| = e^{-4t/T_2}\left|\sum_F \tilde{s}(F)\frac{\sinh(T_s/T_2 - i\pi r T_s(t-F/r))}{2/T_2 - 2i\pi r(t-F/r)}\right|^2, \qquad (54)$$

where the sum runs over the RF frequencies $F$ and $\tilde{s}(F)$ is the amplitude of the RF component of frequency $F$. This expression confirms the expected decay of the signal. It also indicates that the peaks corresponding to the different RF frequencies all have the same width which depends on both the reading chirp duration and the crystal coherence time. Figure 16 displays the expected peak shape for different values of $T_s/T_2$. One observes that for $T_s$ significantly longer than $T_2$, the peak assumes a lorentzian-like shape, strongly asymmetric, and with shifted maximum. On the other hand, the peak is little affected by the coherence time, as long as $T_s < T_2$.

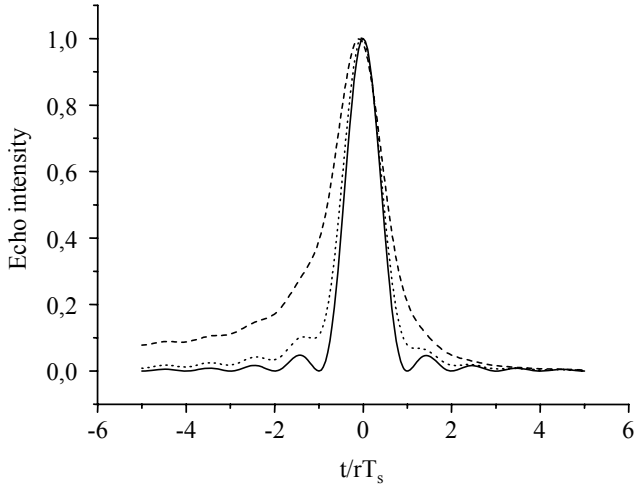


Figure 16. Response peak to a monochromatic RF signal, for $T_2 = \infty$ (continuous line), $T_s$ (dotted line), $T_s/2$ (dashed line).

Let us point out that the exponential decay can be neglected in most cases. According to Eq.(51), the RF spectrum is displayed in a time equal to half the reading pulse duration $T_s$. The exponential decay can therefore be neglected as long as the target resolution $1/T_s$ is more

than the crystal limit $1/T_2$. Since $T_2$ usually lies in the 10 kHz range, one can easily operate with resolutions down to 100 kHz and negligible echo exponential decay.

6.1.6. Engraving chirps

Chirps are now widely used for optical processing of RF signals with optical coherent transients in rare earth doped crystals. The reason is twofold. First a chirp yields a time-to-frequency correspondence that offers considerable versatility in the shaping of a spectrum. Second, the bandwidth and duration required for the chirps are compatible with the capabilities of either a cw laser with chirp capabilities [70], or external modulation of a cw laser [78].

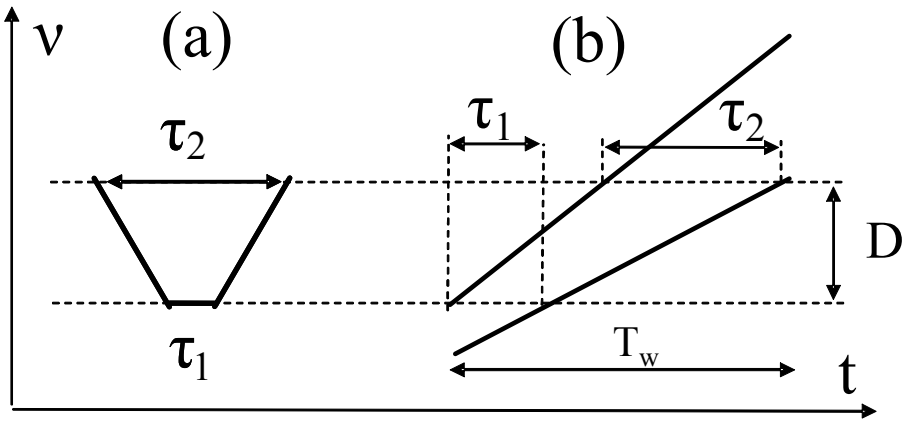


Figure 17. Practical chirps for engraving the dispersive filter in the crystal: (a) two symmetric chirps, (b) two co-temporal chirps of duration $T_w$.

Considering such cw laser sources, one cannot generate short intense pulses. Therefore, the configuration of Figure 15 for engraving the dispersive filter is not practical. Instead one can use the configuration of Figure 17.a. This is the one used in the very first demonstration of the chirp transform algorithm with photon echoes [79]. In this configuration two symmetric chirps with opposite chirp rate $\pm 2r$ engrave the dispersive filter with dispersion rate $1/r$. There is no more short pulse required. However, with this configuration the engraving duration $\tau_2$ must still be shorter than the coherence time $T_2$ of the excited transition in the crystal. Therefore one needs high output power to engrave a dispersive filter with good

efficiency. The configuration of Figure 17.b allows more efficient engraving. It stems from the configuration used in [80] for memory application of photon echoes. In this configuration, one uses two co-temporal chirps with the same duration $T_w$ but different chirp rates. With such an excitation the delay $\tau(\nu)$ recorded by the ions of the crystal still depends on the minimum and maximum delays $\tau_1$ and $\tau_2$, as given by Eq. (48), but is independent of the chirp duration. Consequently, the engraving duration is no longer limited by the coherence time of the crystal but only by the much longer lifetime of the engraving. Therefore, for a given cw laser power, one can put more energy into the filter, and control this energy via $T_w$, independently of the filter dispersion rate. It is this configuration we have used in the experiments reported below. Let us point out that one still needs a fast chirp at readout. This is not a problem from the power point of view since reading must be carried out at lower power than engraving, but still requires a fast chirp source.

## 6.2. Experimental demonstration in $Er^{3+}$:YSO

After a first proof of principle demonstration performed using a $Tm^{3+}$: YAG crystal [79] at a wavelength of 793 nm, the algorithm was tested with a new setup based on a $Er^{3+}$:$Y_2SiO_5$ crystal. Figure 18 shows the relevant energy levels of the erbium ions. One uses the $^4I_{15/2} \rightarrow {}^4I_{13/2}$ optical transition. The choice of the crystal parameters followed from T. Böttger's PhD [81],[82]. We ordered from Scientific Materials a 0.005 % at. doped crystal cut perpendicular to the b axis. The crystal is placed in a magnetic field created between permanent NdFeB magnets. The field was measured to be about 1.1 Tesla. With our crystal cut, the magnetic field is oriented at 135° from the $D_1$ axis which maximizes the coherence time of the transition [81]. The magnetic field is necessary for erbium doped crystals because of Kramers degeneracy. Indeed for ions with an odd number of electrons, the degeneracy of the multiplets cannot be completely lifted by the crystal field Hamiltonian [83]. In the $Y_2SiO_5$ matrix low symmetry sites, a two-fold spin degeneracy remains. Phonon assisted electronic

spin flips of neighbouring $Er^{3+}$ ions is then an important cause of dephasing, limiting the transition coherence time to a few microseconds [53]. An external magnetic field can lift the Kramers degeneracy, eventually freezing the electronic spins in the lower component of the Kramers doublet for high fields. Then one can reach very long coherence times, up to several milliseconds, which is close to the 11 ms lifetime of the $^4I_{13/2}$ level [82]. The wavelength of the transition in site 1 was found to be 1536.2612 nm in vacuum, with a Burleigh 1650 wavemeter, whose calibration was checked against $CH_2$ spectral lines. The apparent discrepancy with the published value of 1536.48 nm in vacuum is actually due to displacement of the transition frequency with applied magnetic field. With the displacement of 0.719 $cm^{-1}$/Tesla measured by T. Böttger and Y.C. Sun [84] for a field oriented at 135° from $D_1$, one computes a field strength of 1.3 Tesla, which is consistent with our direct measurement. We also measured an inhomogeneous full width at half maximum of 1.2 GHz. This larger value as compared to the one found by Böttger is due to magnetic field inhomogeneities.

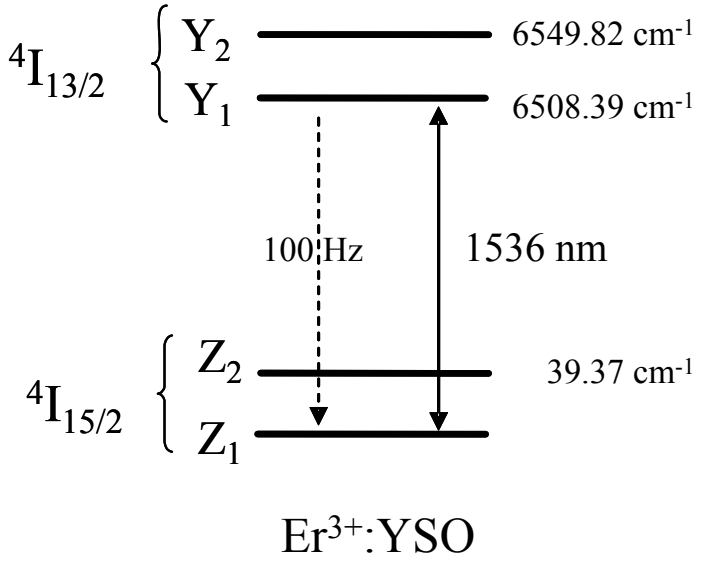


Figure 18. Energy levels of the $Er^{3+}$ ion, showing the first two levels of the ground and excited Stark multiplets in the YSO matrix

A new wavelength gives the opportunity to test new laser sources for photon echoes. The following experiments were performed with a fiber laser from Koheras. Based on a

distributed feedback fiber laser followed by an amplification stage, it yields 6 mW of polarization maintained output. With this laser, Koheras measured the linewidth of the output beat from an asymmetric Mach Zehnder with 120 μs delay, and the result was a few kHz. Such a measurement does not directly yield the laser linewidth, and what is more, does not give information on frequency jitter occurring on a time scale longer than the Mach Zehnder asymmetry. However, fiber lasers are expected to, and actually do, as experiments below demonstrate, have much better frequency stability than the diode lasers used mainly in photon echo experiments. The price to pay is the lack of chirping capabilities of our fiber laser. But the research for integrated chirped lasers has already begun.

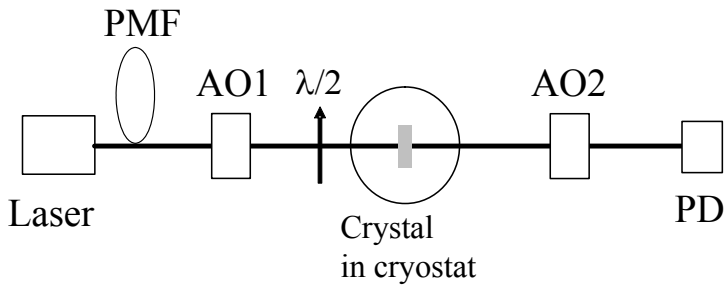


Figure 19. Experimental setup sketch. PD: photodiode, AO: acousto-optic cell, PMF: polarization maintaining fiber, $\lambda/2$: half wave plate.

The setup for the first echo experiments is a simple collinear setup sketched in Figure 19. The laser beam is collimated and focused in an acousto-optic AO1 (custom model by A&A, with >50% diffraction efficiency over a 40 MHz RF-frequency range). Controlled by an arbitrary waveform generator (Tektronics AWG520), it is used to produce the chirps, as well as amplitude modulation of the laser beam. The beam is focused to a spot of 25 μm waist in the crystal which is maintained at about 1.5 K. The available power is typically 1-2 mW in front of the cryostat. A half wave plate before the crystal controls the polarization of the beam. After the cryostat the beam is then gated by AO2, which protects the photo detector (New Focus Mod 1811, 125 MHz bandwidth). The photodetected signal is digitized and displayed by an oscilloscope with 2 GS/s sampling rate and 10 kpoints of memory depth. In

the setup, the fiber laser output, AO1, the crystal, AO2, and the photodiode, are all in image planes with respect to each others.

The Fourier transform of a square function is a cardinal sine. We checked this basic property with our photon echo Fourier transformer. We used the co-temporal chirp configuration of Figure 17.b for engraving, with parameter values $T_w = 30\mu s$, $\Delta = 40MHz$, $\tau_1 = 0$, $\tau_2 = 12\mu s$. This double chirp was programmed on a single output of the AWG, which was fed to AO1. The power at engraving was 1.8 mW in front of the cryostat. The reading pulse is a simple chirp of duration $T_s = 3\mu s$, spectrally centered in the dispersive filter spectral band (cf. Figure 15). The engraving plus reading sequence was cycled at 100 Hz, which was found to optimize the signal strength, giving about twice the signal strength at 10 Hz cycling rate. For higher repetition rates the signal strength was about stationary up to 300 Hz and then slowly decreased down to zero. Such a signal decrease at high cycling rate is expected since the atomic system is a two level system. A precise study of the accumulated engraving regime with our experimental system remains to be done. Still, the gain on signal strength observed under accumulation indicates that laser frequency stability is sufficient for this accumulation regime to work, which is necessary from the application point of view.

Figure 19.a shows the detected echo signal in logarithmic scale while Figure 19.b shows the fit by the $\sin c^2$ function. A very good fit is obtained down to the last detectable sidelobe with sinc width of 100 ns, as expected. This demonstrates faithful Fourier transform with a power optical dynamic range of 27 dB.

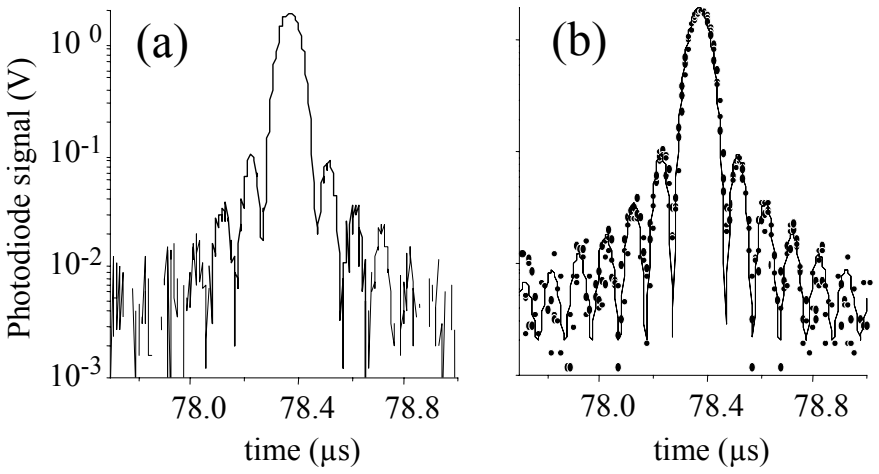


Figure 20. Power spectrum of an input 3 μs square signal as given by the photon echo chirp transform, in log scale. The signal was averaged over 16 shots. The optical power was 2 mW. Successive engraving and reading cycles were repeated at 100 Hz. (a) experimental signal. (b) fit (line) of the same experimental record (dots) by the expected $\mathrm{sinc}^2$ function.

We then tested the response of the Fourier transformer to a multi-frequency RF signal. The engraving sequence was the same as above with $\tau_1 = 0.2\mu s$ and $\tau_2 = 15.2\mu s$. The small $\tau_1$ value was chosen so that the zero-RF-frequency peak is visible in the echo to serve as a frequency reference. We used the single sideband chirp configuration of Figure 15.b for reading, with a power of 0.3 mW in front of the cryostat.

Figure 21 presents the spectrum of an input RF signal $s(t) = 0.3 + \sum_i \sin(2\pi F_i t)$ with 10 frequencies $F_i$ spanning a 13.4 MHz interval, and lasting 7.5 μs. The observed peak width of $39 \pm 2ns$, where the error is due to the low time resolution of the recording, compares well with the $1/rT_s = 38ns$ value. The peaks are also situated at the expected positions. Apart from peak-to-peak height fluctuations the spectrum analyzer response is rather flat over its bandwidth. This was obtained via tuning of the Bragg angle of the gate cell AO2 which was found to modify considerably the overall shape of the response. This stems from the fact that the echo is on a chirped optical carrier which is also angularly rotating and the AO2 cell diffraction efficiency is not a flat function of incident angle. AO1 Bragg angle tuning was also found to alter the peak-to-peak amplitude fluctuations. This seems to indicate that the peaks

unevenness is due to the modulation process in AO1. We checked with dedicated experiments that this was indeed the case [85].

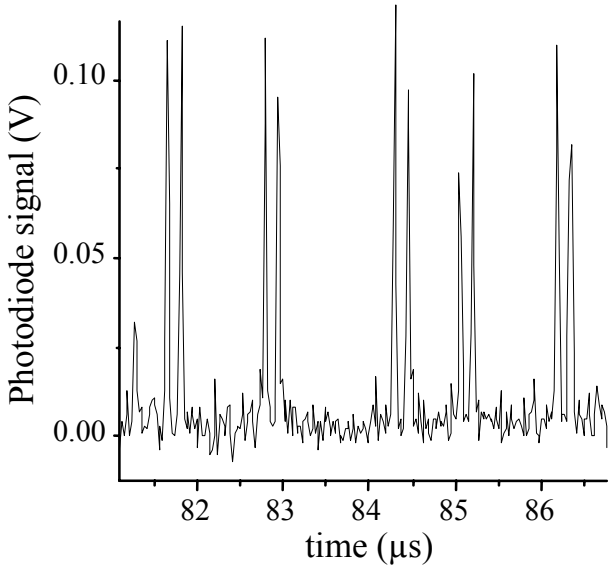


Figure 21. Experimental spectrum of an input RF signal containing 10 frequencies. Single shot record. Time translates into frequency with the coefficient 2.67 MHz/μs. The first peak on the left corresponds to the optical carrier (RF frequency =0).

Higher resolution was then tested. Figure 22.a and c (respectively Figure 22.b and d) show records from single sideband experiment with $T_w = 100\mu s$, $\Delta = 40MHz$, $\tau_1 = 0.2\mu s$, $\tau_2 = 40.2\mu s$ (resp. 50.2 μs), 10 Hz cycling rate, and a power of 1.8 mW at engraving. The reading signal, with 0.3 mW of power, lasted 20 μs (resp. 25 μs) and contained 12 frequencies spanning a 20 MHz bandwidth, set so that no second order harmonic combination of any two frequencies coincides with another frequency. The peak width is 48 ns, again in agreement with the computed $1/rT_s$ value, and the peaks are all at expected positions. This corresponds to a $1/T_s$ resolution of 50 kHz for the records of Figure 22.a and c, and 40 kHz for the records of Figure 22.b and d. It demonstrates a time bandwidth product of 500.

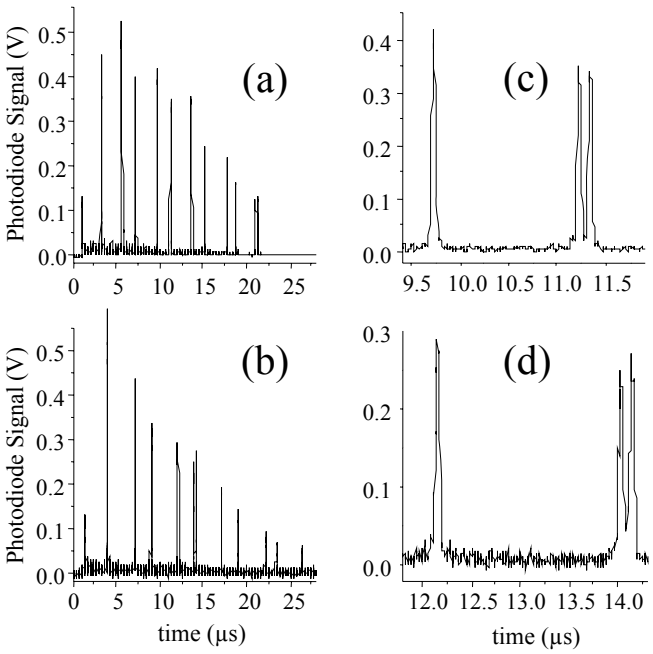


Figure 22. High resolution single side band spectra given by the photon echo spectrum analyzer. The input RF signal contains 12 RF frequencies spanning a 20 MHz wide interval. (c) is a zoom on part of (a) and corresponds to 50 kHz resolution. (d) is a zoom on part of (b) and corresponds to 40 kHz resolution.

One notices a decay of the signal as a function of time. These recordings were taken after checking the correct Bragg tuning of the gate AO2. Therefore the observed decay should be attributed to the coherence time of the crystal. Actually, the observed decay along the 20 μs (resp. 25 μs) duration of the signal would correspond to a coherence time of 50 μs. This is compatible with previous measurements we made.

## 6.3. Discussion

The above results fully demonstrate the high resolution capability of the photon echo chirp transform spectrum analyzer. However this architecture has yet to be demonstrated over multi-GHz bandwidth. The difficulty is then to produce the necessary chirps. If one resorts to electronic modulation to produce these chirps, the photon echo approach adds little as compared to surface acoustic wave devices. Indeed, in order to reach the 10 GHz bandwidth capability, one must be able to produce the corresponding chirps using frequency agile lasers. Because these chirps must span the 10 GHz in a few microseconds only, this puts severe

constraints on laser technology. All the more since the chirp linearity must be very good, the echo signal resulting from coherent superposition of the whole excited bandwidth. Laser technology is advancing in this direction. Demonstration of the photon echo chirp transform over a 1 GHz bandwidth using a frequency agile laser is a challenging goal, whose success would open the way to many other applications.

As compared to chirp transform spectrum analyzer developed with SAW dispersive delay lines, the photon echo chirp transform approach has two main advantages. First, the bandwidth capability is much greater since rare earth doped crystals inhomogeneous bands are several tens of GHz wide. Let us point out that the limited bandwidth or the Erbium doped crystal used in our first demonstration is not representative. YSO crystals co-doped with Er and Eu have bandwidth greater than 10 GHz with very similar coherence properties. The Er:LiNbO3 crystals has an inhomogensous width of 270 GHz [82]. The other advantage is flexibility. Whereas the bandwidth and resolution of a SAW chirp transform analyzer is fixed at construction, the bandwidth and resolution of our analyzer can be modified in a short time, thanks to the limited lifetime of engraving in the crystal.

One may also point out the features of this spectrum analyzer as compared to the other architectures discussed here. The chirp transform analyzer gives fastest access to the RF spectrum, since that spectrum is displayed in a time limited only by the spectral resolution. The immediate drawback is that detection of the spectrum requires a bandwidth equal to the RF signal bandwidth, which is not favorable to dynamic range. From an engineeering point of view, the optical setup is rather straightforward because signal processing is in the time-frequency domain only. The main technological challenge lies in laser technology.

# 7. Frequency agile laser technology

## 7.1. Requirements

Development of the different hole-burning spectrum analyzers presented above, and more generally, of hole-burning based optical processors, relies strongly on laser technology. More specifically one needs high spectral purity, rapidly tunable, monochromatic lasers, so-called frequency agile lasers. In the following, we discuss the laser requirements for the three spectrum analyzers presented above, considering the aim of 10 GHz bandwidth and 1 MHz resolution. Then we describe our present laser architectures. Subsection 7.3 is devoted to the techniques we developed to measure the chirp spectral purity. Finally subsection 7.4 mentions present laser technology developments for applications to RF signal processing.

In the photographic architecture described in Section 3, the laser must scan the absorption band of the crystal so as to probe the engraved RF spectrum. The sweeps must cover a bandwidth of typically 10 GHz, in a time of typically 1 ms, since the engraving lifetime is 10 ms. Obviously, the spectral resolution is limited by the laser linewidth during the scan. The absolute precision of the retrieved RF spectrum depends on the linearity of the sweep. An absolute precision of 1 MHz over a 10 GHz wide sweep is a severe constraint.

For the rainbow analyzer (see Section 5), the constraints are a bit more severe. In this architecture, the laser frequency must be linearly scanned over 10 GHz, synchronously with the angular scanning of the engraving beams. This engraves in the crystal the set of monochromatic Bragg gratings which make the frequency-to-angle processor used for angular separation of the RF spectral components. Here again the precision of the frequency-to-angle law engraved in the crystal critically depends on the linearity of the laser sweep. We therefore have the same linearity constraint as for the photographic analyzer. In addition, since engraving must be performed within the grating lifetime, the same chirp rate as for the photographic analyzer is required. However, one also has to consider the necessity to refresh

the gratings. This forces one to repeat the engraving cycles at a rate higher than the gratings decay rate. Then the engraved processor is the result of accumulation of successive cycles. With a 2 kHz cycling rate one typically accumulates 20 cycles in the 10 ms grating lifetime. Supposing the chirps are perfectly linear, should the laser frequency shift between two successive sweeps, this shifts the frequency-to-angle law. As a result, not only is the spectral resolution degraded, but also the diffraction efficiency of the accumulated gratings. Hence a central frequency stability constraint is added to the linearity constraint.

The photon echo chirp transform spectral analyzer is by far the most demanding, mainly because in this architecture the signal results from coherent addition of the atomic response from the whole analyzer bandwidth. For this architecture, one need laser chirps both at engraving and at reading. Let us first consider the programming stage. Using the co-temporal chirp approach discussed in Section 6.1.6, the laser frequency must sweep the whole analyzer bandwidth in a time limited by the grating lifetime. We therefore need the same chirp rate, say 10 GHz in typically 1 ms, as required for the rainbow and the photographic analyzers. Linearity is also required. One must also consider the necessary refreshing, as for the rainbow analyzer, which again adds the constraint of central frequency stability. At reading, one needs a laser chirp that covers the whole bandwidth in a time given by the inverse of the resolution. This means covering 10 GHz in a few microseconds, only, a challenging task indeed. Obviously, linearity is required.

Let us point out that the linearity requirement actually does not mean the same for the chirp transform as for the other two analyzers. In the latter ones, phase defaults in the laser chirps have limited consequence since the different spectral channels are treated independently. Such defaults have drastic consequences in the chirp transform analyzers since the signal coherently combines atomic response from the whole analyzer spectral bandwidth. Indeed a phase continuous chirp is required.

## 7.2. Electro-optic tuning of diode laser extended cavity

Diode lasers have many interesting features such as compactness, high gain and high wall plug efficiency. However, their spectral linewidth is usually several tens of MHz. Using the diode as a mere gain medium in an external cavity closed by a diffraction grating is the usual way to lower the laser linewidth to a few tens of kHz or below. In addition, the diffraction grating is a convenient way to control the laser frequency. Mechanically moving the grating in a well controlled way produces laser frequency mode-hop-free tuning over several tens of nm. Piezo-electrically controlled grating movements can produce frequency sweeps a few tens of GHz wide at a few hundred hertz repetition rate. Our linearity constraint forbids the use of such sweeping solutions. Instead, because of its fast response and high linearity, we chose to rely on the electro-optic effect for frequency agility.

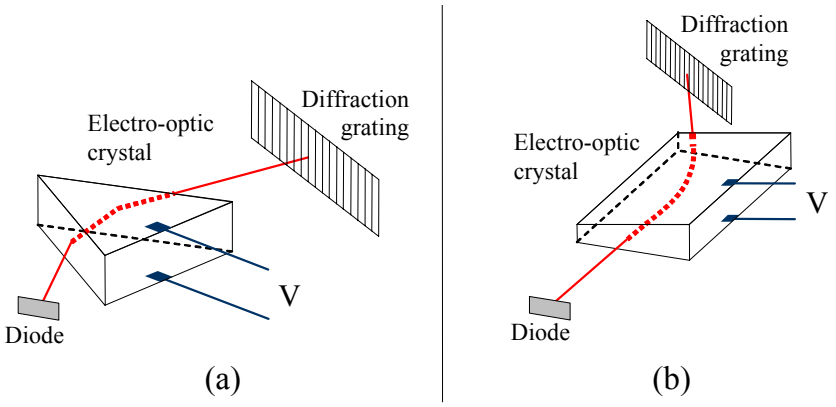


Figure 23. Principle of extended cavity diode laser with intracavity electro-optic crystal for fast mode hop free frequency tuning. (a) Prism type cavity. (b) Wedge type cavity.

Figure 23 gives the principle of the Littrow type cavities we have developed. In Figure 23 a, the intracavity electro-optic crystal is cut as a prism. Applying a voltage between the crystal faces modifies the refractive index, which has two consequences. It shifts the laser cavity mode frequency $\nu$ according to

$$\frac{\Delta\nu}{\nu} = \frac{\Delta L}{L} = e\frac{\Delta n}{L}, \qquad (55)$$

where e is the beam path length in the crystal and L is the total optical length of the cavity. It also changes the angle of incidence of the beam on the grating, shifting the Littrow wavelength according to

$$\frac{\Delta\nu}{\nu} = \frac{(d\theta/dn)\Delta n}{\tan\theta}, \tag{56}$$

where θ is the angle of incidence on the grating. In order to perform mode-hop-free frequency sweeps, the two variations must be the same, which determines the crystal geometrical parameters versus the cavity optical length. With the prism set in the minimum deviation orientation, the mode hop free condition imposes

$$e/L = \frac{2\sin(\alpha/2)}{\tan\theta\sqrt{1-n^2\sin^2(\alpha/2)}} \quad . \tag{57}$$

First demonstration of this principle was performed in 2000 [70]. A similar idea was later developed [58], in which the prism is replaced by a wedge (see Figure 23b). Applying a voltage to the crystal then results in an index gradient. This again shifts the laser cavity mode according to Eq. (55), and also deviates the beam incidence on the grating via the mirage effect according to Eq. (56) where $d\theta/dn$ now depends on the wedge angle $\varepsilon$ and thickness $h$. Mode hop free tuning is achieved if

$$\varepsilon = h\tan\theta/L\,. \tag{58}$$

Whereas the first laser built to demonstrate the prism approach principle was a crude one, better engineering work was performed, in collaboration with Lund University, to develop a laser based on the wedge principle. Based on a LiTaO3 crystal wedge and antireflection coated diodes from JDS-SDL and operating around 795 nm these lasers can sweep over up to 50 GHz wide intervals, with an electro-optic sensitivity of 12 MHz/V. The laser sweep rate is limited by the high voltage source performance. One easily performs 10 GHz wide chirps in 1 ms. Several copies of the same model were built, which have been used to demonstrate the rainbow spectral analyzer, and later the spectrum photography analyzer. Experiments using

the rainbow analyzer in accumulation mode showed that the laser sweeps can be repeated with a precision of about 500 kHz over a 10 ms time. The laser coherence time and technical noise were characterized with dedicated experiments described in the next section.

One copy of this laser also proves very useful in coherent control experiments of thulium ions in a YAG host [86]. In these experiments, the laser frequency is locked to a high finesse cavity using the Pound-Drever-Hall technique [87]. The intracavity crystal was found to be a very convenient element on which to close the feedback loop. Thanks to the DC-2 MHz bandwidth of the crystal's electro-optic response function, a single loop was implemented, instead of the usual combination of a low-frequency loop (acting for example on a piezoelectric transducer) and a high-frequency loop (acting for example on the diode injection current).

## 7.3. Laser chirp spectral purity characterization

As we have seen above, the spectral purity of the laser during the chirp determines the resolution and the frequency precision of the RF spectral analysis. Ideally, we need to maintain the laser frequency deviation from a perfectly linear chirp lower than 1 MHz. In order to fulfill this condition, a complete measurement of laser frequency noise during the chirp is necessary. Two different families of phase errors occurring during the laser chirp can be distinguished. First, deterministic errors, such as, e.g., the non-linearities of the chirp or some extra frequency modulations have to be isolated. Second, stochastic errors, such as the phase random walk induced by the spontaneous emission or the technical $1/f$ frequency noise, have to be characterized. This noise exists of course in the case of fixed frequency lasers and can be measured with well-known techniques [[87]-[90]]. The problem here is to measure this noise while the average frequency is swept rapidly.

Some experiments dealing with the phase noise characterization of frequency-chirped CW lasers have already been reported [[91]-[95]]. However, these techniques are either not

adapted to the values of the chirp rates and amplitudes used here or are not sensitive enough to be able to deal with the different kinds of noise investigated here. Consequently, we needed develop a specific experiment for the complete characterization of single linear frequency chirps in the range necessary for RF signal processing (10 GHz in 1 ms or 1 μs) with the required resolution (1 MHz) [96].

For a chirped laser operating above threshold with constant amplitude, the phase fluctuations are the major causes of spectral impurity. A well-known process to detect the phase fluctuations of usual, i. e., fixed frequency lasers is provided by path-difference interferometers. This is why we choose here also a self-heterodyne interferometry technique for characterizing the deterministic and stochastic phase errors of a rapidly chirped laser. This consists of an unbalanced Mach-Zehnder interferometer with a time delay $\tau_d$ between the two paths, as schematized in Figure 24.

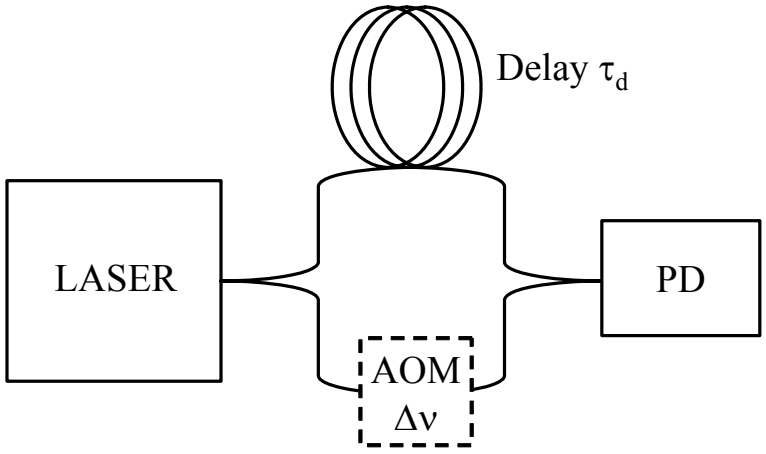


Figure 24. Principle of the unbalanced interferometer. PD: photodetector; AOM: acousto-optic modulator creating a frequency shift $\Delta\nu$.

At the laser output and in the absence of noise, the electrical field can be expressed as

$$E(t) = \mathscr{E}(t) + c.c. = E_0 e^{2i\pi\left(\nu_0 t + \frac{1}{2}rt^2\right) + i\phi_0} + c.c., \tag{59}$$

where $E_0$ is the light field amplitude which we suppose constant, $\nu_0$ is the average optical frequency, $r$ is the chirp rate value and $\phi_0$ is a constant phase. In the unbalanced Mach-Zehnder interferometer schematized in Figure 24, the laser beam is split in two arms. One of

them experiences a delay $\tau_d$ while the other is frequency shifted by an acousto-optic modulator operating at frequency $\Delta\nu$. If the contrast is supposed to be equal to 1, the recombination of these two beams at the output of the interferometer leads to the following field:

$$E_T(t) = \frac{1}{\sqrt{2}}\left[\mathscr{E}(t)e^{-2i\pi\Delta\nu t} + \mathscr{E}(t-\tau_d) + c.c.\right]. \tag{60}$$

Consequently, the detected intensity is

$$I(t) = 2E_0^2\left[1+\cos\left(2\pi f_b t + 2\pi\nu_0\tau_d - \pi r\tau_d^2\right)\right], \tag{61}$$

where $f_b = r\tau_d - \Delta\nu$ is the beat signal frequency. We notice that $f_b$ is a linear function of the chirp rate $r$. The laser chirp rate $r$ can consequently be determined by a simple Fourier analysis of the beat note signal. Of course, the typical resolution of the resulting spectrum will be of the order of $1/T$, where $T$ is the duration of the considered chirp. However, the precision on the measurement of $r$ can be adjusted by modifying the delay $\tau_d$. Moreover, even for low values of $\tau_d$, the signal can be shifted out of the low frequency noise region to higher frequencies thanks to the acousto-optic modulator frequency $\Delta\nu$.

As we have just seen, a perfect chirp will lead to a beatnote at frequency $f_b = r\tau_d - \Delta\nu$ at the output of the interferometer. Any discrepancy with respect to a perfect beat note will reveal the existence of an error. In order to illustrate the sensitivity of this technique, we choose two examples: a deterministic error and a stochastic error.

A first example of result is reproduced in Figure 25. This has been obtained with the external cavity diode laser at 793 nm that we used for the spectral photographic analyzer (see Section 3) and the rainbow analyzer (see Section 5). Figure 25 (a) is the FFT of the beat signal obtained at the output of the unbalanced interferometer for a chirp amplitude $\Delta\nu_{laser} = 10\,\mathrm{GHz}$ in a duration $T = 20$ ms. The delay of the interferometer is $\tau_d = 150$ ns. The width of this spectrum is much broader (of the order of a few kHz) than what could be

expected from the resolution of the FFT ($1/T = 50$ Hz), indicating an important deviation of the laser instantaneous frequency with respect to a perfectly linear chirp. To analyze this deviation, one can divide the 20 ms-long signal in ten successive records lasting 2 ms each. The FFT spectra of these ten successive records are shown in Figure 25(b). As can be seen in Figure 25(c), the average beat frequency $f_b$ increases quasi-linearly as a function of time during the 20 ms-long chirp. Consequently, the laser instantaneous frequency can be modeled by the expression $\nu(t) = \nu_0 + rt + \alpha t^2$, with $r = 0.47$ THz/s and $\alpha = 1.5$ THz/s². In this case, this error was due to a bad alignment of the grating closing the laser cavity.

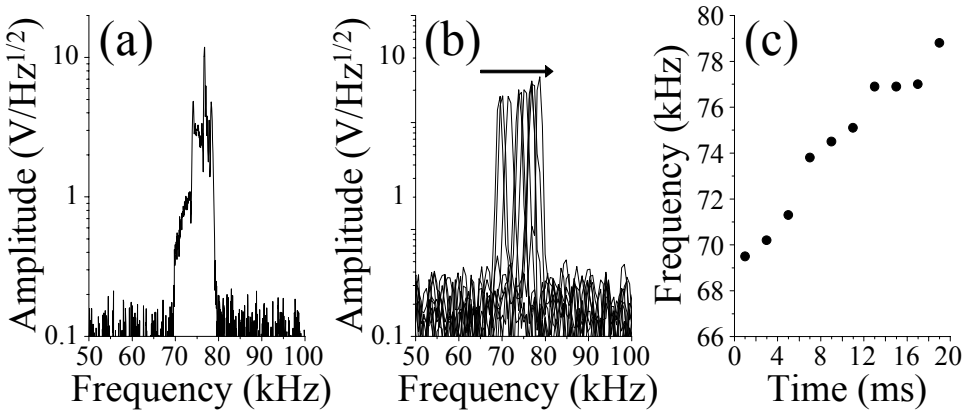


Figure 25. Experimental result for a 20-ms-long chirp of amplitude 10 GHz presenting a variation of *r*. The delay is $\tau_d = 150ns$. (a) Spectrum of the whole signal. (b) Ten spectra corresponding to the ten successive 2-ms-long parts of the whole signal. (c) Corresponding evolution of the averaged beat note frequency versus time. Each point corresponds to a 2-ms duration sample.

The result of Figure 25 illustrates the capability of our unbalanced interferometer to detect deterministic deviations of the laser chirp with respect to perfectly linear ones. We have also put into evidence the ability of this system to detect other types of deterministic errors, such as an, extra sinusoidal frequency modulation superimposed on the linear frequency chirp. This type of error leads to frequency-modulation side bands on the FFT of the beat signal, allowing a precise measurement of the amplitude and frequency of this spurious modulation [96]. One can show that the precision on the measurement of such deterministic errors is better than 1MHz, as required.

Another illustration of the usefulness of this technique is illustrated by its ability to detect stochastic laser phase fluctuations during the chirp. As with most lasers, we can expect the lasers described above (see Section 7.2) to be affected by two main types of frequency noise: i) white frequency noise due to spontaneous emission which leads to the Schawlow-Townes linewidth in the case of usual stable frequency lasers and ii) low frequency (typically 1/*f*) technical frequency noise induced by mechanical or acoustic variations of the laser cavity length. In both cases, we can write the instantaneous phase of the linearly chirped laser as

$$\Phi(t) = 2\pi\left[\nu_0 t + \frac{r}{2}t^2\right] + \phi(t). \tag{62}$$

Here, $\phi(t)$ can represent both the white quantum and the low-frequency technical noise. At the output of the interferometer the optical intensity incident on the detector can be written as

$$I(t) = 2E_0^2\left(1 + \cos\left[2\pi f_b t + \psi_0 + \phi(t) - \phi(t-\tau_d)\right]\right). \tag{63}$$

A sine wave is observed at the output of the photo detector with an average frequency $f_b$. To obtain the spectrum of this signal, we need to calculate the auto-correlation function of $I(t)$ and apply the Wiener-Khinchin theorem. The auto-correlation function is given by

$$R_I(t,\tau) = \langle I(t)I(t+\tau)\rangle \ , \tag{64}$$

where the brackets $\langle\ \rangle$ denote ensemble averaging. This leads to

$$R_I(t,\tau) = 4E_0^4 + 2E_0^4\langle\cos H(t,\tau)\rangle\cos(2\pi f_b\tau) \ , \tag{65}$$

where we have defined

$$H(t,\tau) = \phi(t+\tau) - \phi(t) - \phi(t+\tau-\tau_d) + \phi(t-\tau_d) \ . \tag{66}$$

$H(t,\tau)$ depends on the optical phase at four different times. We suppose that the phase jitter defined by

$$\Delta\phi(t,\tau) = \phi(t+\tau) - \phi(t) \tag{67}$$

is a zero-mean stationary Gaussian process. Then the dependence in $t$ disappears in the moments of $H(t,\tau)$, and the auto-correlation function of the optical intensity can be written as

$$R_I(\tau) = 4E_0^4 + 2E_0^4 \, \mathrm{e}^{-\frac{1}{2}\left\langle H^2(t,\tau)\right\rangle} \cos(2\pi f_b \tau) \ . \tag{68}$$

The Fourier transform of $R_I(t)$ leads to the spectrum of the intensity detected at the output of the interferometer. Let us first suppose that the only noise occurring in the frequency chirped laser is white quantum noise. In this case, the auto-correlation of the frequency error is given by

$$\left\langle \dot{\phi}(t+\tau)\,\dot{\phi}(t)\right\rangle = \frac{1}{\tau_c}\delta(\tau), \tag{69}$$

where $\tau_c$ is the laser coherence time. From Eqs. (66) and (67), one can express $R_I(\tau)$ as a function of the phase jitter as

$$H(t,\tau) = \Delta\phi(t,\tau) - \Delta\phi(t-\tau_d,\tau) \ . \tag{70}$$

Using Eq.(69), this leads to

$$\left\langle H^2(t,\tau)\right\rangle = \begin{cases} 2|\tau|/\tau_c & \text{for } |\tau| < \tau_d, \\ 2\tau_d/\tau_c & \text{for } |\tau| > \tau_d. \end{cases} \ . \tag{71}$$

This can be used together with Eq. (68) to obtain

$$R_I(\tau) = 4E_0^4 + \begin{cases} 2E_0^4 \cos(2\pi f_b \tau)\,\mathrm{e}^{-|\tau|/\tau_c} & \text{for } |\tau| < \tau_d, \\ 2E_0^4 \cos(2\pi f_b \tau)\,\mathrm{e}^{-\tau_d/\tau_c} & \text{for } |\tau| > \tau_d. \end{cases} \tag{72}$$

Consequently, the power spectral density of the detected signal is given by the Fourier transform of Eq. (72)

$$\begin{aligned} S_I(\omega) = {} & 4E_0^4\delta(\omega) + E_0^4 \, \mathrm{e}^{-\tau_d/\tau_c}\,\delta(\omega - 2\pi f_b) \\ & + E_0^4 \, \mathrm{e}^{-\tau_d/\tau_c} \frac{\tau_c/\pi}{1+(\omega-2\pi f_b)^2 \tau_c^2} \left[ \mathrm{e}^{\tau_d/\tau_c} - \cos(\omega - 2\pi f_b)\tau_d - \frac{\sin(\omega-2\pi f_b)\tau_d}{(\omega-2\pi f_b)\tau_c} \right] \\ & + \{ f_b \to -f_b \}. \end{aligned} \tag{73}$$

This result is similar to the self-heterodyne spectrum obtained for laser sources operating at fixed frequency [[88]-[90]], except for the frequency shift $f_b$ which varies with the chirp rate. Consequently, the quantum frequency noise of our chirped laser can be obtained as usual by taking $\tau_d$ as long as possible in order to favor the Lorentzian part of Eq. (73), which is just the image of the Lorentzian Schawlow-Townes broadening, with respect to the Dirac term. We have used this technique to isolate the white part of the stochastic frequency noise of our frequency agile lasers while it is chirped. As expected, we have checked that the Schawlow-Townes linewidth of the laser is not modified by the fact that the laser average frequency is chirped [95].

Let us now turn to the case of a low-frequency noise affecting the laser frequency, induced for example by mechanical or acoustic noise. We suppose in the following calculation that this noise is the predominant process, with respect to which all other noise can be neglected. If we choose the interferometer delay $\tau_d$ short enough with respect to the characteristic time of variation of the laser frequency noise $\dot{\phi}(t)$, i. e., with respect to the laser frequency noise coherence time, the following simplification can be used:

$$\phi(t) - \phi(t - \tau_d) \approx \tau_d \dot{\phi}(t) \ . \tag{74}$$

This can be used to simplify Eq. (66), leading to

$$H(t,\tau) = \tau_d \left( \dot{\phi}(t+\tau) - \dot{\phi}(t) \right) . \tag{75}$$

To obtain the auto-correlation function of the detected intensity, one needs to calculate the variance of $H$

$$\left\langle H^2(t,\tau) \right\rangle = 2\tau_d^2 \left[ \sigma_{\dot{\phi}}^2 - R_{\dot{\phi}}(\tau) \right], \tag{76}$$

where $R_{\dot{\phi}}(\tau)$ is the auto-correlation function of the frequency noise $\dot{\phi}(t)$ and where we have supposed that the variance $\sigma_{\dot{\phi}}^2$ of $\dot{\phi}(t)$ is finite. In the case of $1/f$ noise, this latter condition

can be easily fulfilled by bounding the frequency noise spectrum to a finite interval $[\omega_{\min}, \omega_{\max}]$ with $\omega_{\min} > 0$. Equation (68) then leads to

$$R_I(\tau) = 4E_0^4 + 2E_0^4 \, \mathrm{e}^{-\tau_d^2 \sigma_{\dot{\phi}}^2} \, \mathrm{e}^{\tau_d^2 R_{\dot{\phi}}(\tau)} \cos(2\pi f_b \tau). \tag{77}$$

An analytical expression of the spectrum can be obtained if $\tau_d$ is short enough to fulfill the following condition

$$\left| \tau_d^2 R_{\dot{\phi}}(\tau) \right| \leq \tau_d^2 \sigma_{\dot{\phi}}^2 << 1 \, . \tag{78}$$

Then the exponential term $\exp\left[\tau_d^2 R_{\dot{\phi}}(\tau)\right]$ in Eq. (77) can be expanded to first order. The Fourier transform of Eq. (76) can be expressed as

$$S_I(\omega) = 4E_0^4 \delta(\omega) + E_0^4 \, \mathrm{e}^{-\tau_d^2 \sigma_{\dot{\phi}}^2} \left[ \delta(\omega - 2\pi f_b) + \tau_d^2 S_{\dot{\phi}}(\omega - 2\pi f_b) \right] + \{ f_b \to -f_b \} \, . \tag{79}$$

This equation shows that the interferometer has transferred the low-frequency frequency noise to the base of the Dirac peak created by the beat note at $f_b$. This is illustrated by the experimental result of Figure 26. We have just seen [see Eq. (74)] that to measure the spectrum of such a frequency noise, we must choose the delay $\tau_d$ of the interferometer much shorter than the typical timescale of the variations of the instantaneous laser frequency. This is why we choose here a rather small interferometer path difference using a 20 m-long fibre, leading to $\tau_d$ = 100 ns. Contrary to the results of Figure 25 which led to the measurement of deterministic frequency errors, we keep the acousto-optic frequency shifter at 80 MHz, in order to shift the spectrum far from the zero frequency. In order to maintain a sufficient dynamical range for the measurements, we have to analyze the signal using the spectrum analyzer. The resolution we want (1 kHz) obliges us to work with very slow chirps only ($T$ = 2.5 s).

Figure 26 (a) shows the typical spectra (here with $r = 0$) that we obtain with a resolution bandwidth of 30 kHz, when the laser is not chirped. Three different parts can be

distinguished in this spectrum: i) the Dirac term at $f_b$; ii) the oscillations due to the white frequency noise and given by Eq. (73), that are consistent with the value $\tau_c = 20\ \mu s$ determined from other measurements; and iii) a broadening, together with extra lines at the base of the Dirac peak, over a bandwidth of the order of 500 kHz. This last low-frequency component is the one we wish to investigate here. As required [see the discussion of Eq. (74) ], its bandwidth is much smaller than $1/\tau_d = 10^7\ s^{-1}$ . We hence zoom on a 2 MHz bandwidth around 80 MHz with a resolution bandwidth of 1 kHz, leading to the spectrum of Figure 26(b). We can clearly see the extra noise component lying at the base of the Dirac peak and on top of the background noise given by the white noise component of the self-heterodyne spectrum. We use Eq. (79) to extract the low-frequency component of the power spectral density $S_{\delta\nu}(\omega)$ of the instantaneous frequency error $\delta\nu = \dot{\phi}/2\pi$ . This leads to the spectrum of Figure 26(c). This noise is quite well fit by a $1/f$ law between 5 kHz and 400 kHz, suggesting a technical origin. The total power of this noise, which gives the variance $\sigma_{\delta\nu}$ of the frequency due to this noise component, is given by the area below the spectrum of Figure 26(c) and is of the order of 18 kHz. This shows that $\tau_d \sigma_{\dot{\phi}} = 2\pi\tau_d \sigma_{\delta\nu} \approx 10^{-2} << 1$, as required to derive Eq. (79). The peak at 864 kHz should not be attributed to the laser frequency: it is due to the 'Radio Bleue' broadcasting transmitter of Villebon-sur-Yvette, close to our laboratory. Now, at very slow chirp $r = 1.5$ MHz/ms ($\Delta\nu_{laser} = 3.75$ GHz in $T = 2.5$ s), the central part of the self-heterodyne spectrum becomes the one of Figure 26(d). After transformation using Eq. (79), we obtain the power spectral density of the instantaneous frequency noise of Figure 26(e). The noise is larger than in the case of Figure 26(c), with a variance $\sigma_{\delta\nu}$ of the order of 60 kHz. This is still consistent with the hypothesis $\tau_d \sigma_{\dot{\phi}} << 1$ . The increase of the low-frequency noise has been observed to be independent of the value of $r$, in the range of small values of $r$ achievable with the present

experiment. Actually, the extra noise observed in Figure 26(e) with respect to Figure 26(c) is due to the high-voltage amplifier which amplifies the ramp applied to the electro-optic crystal. This illustrates the high sensitivity of the present setup.

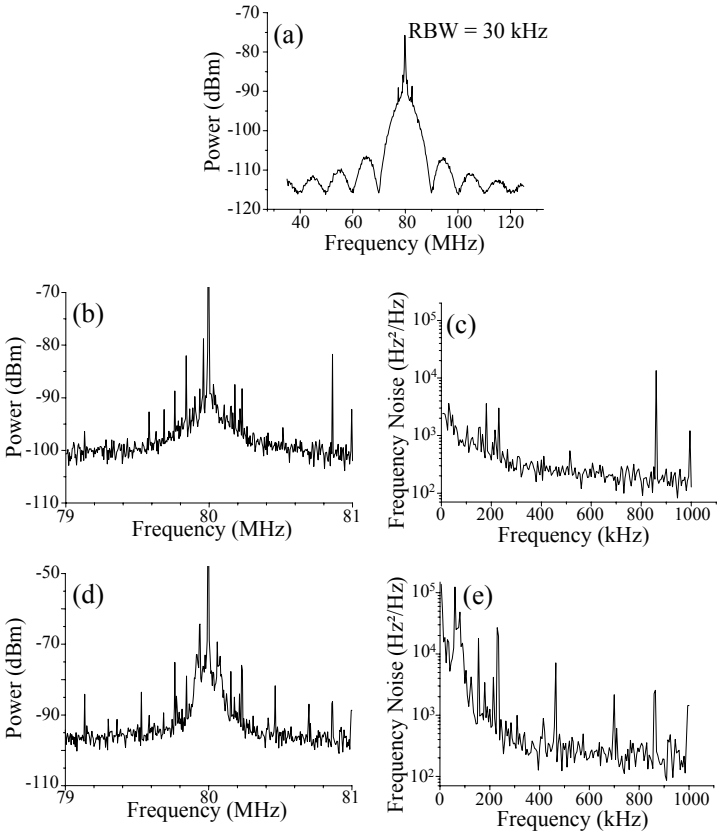


Figure 26. (a) Experimental self-heterodyne spectrum for $\tau_d = 100$ ns, $\Delta\nu = 80$ MHz, and $r = 0$ recorded with a 1 GHz bandwidth photodiode. (b) Zoom on the central part of the self-heterodyne spectrum with a resolution bandwidth RBW = 1 kHz and for $r = 0$. (c) Instantaneous frequency spectrum extracted from (b). (d,e) Same as (b,c) for $r = 1.5$ GHz/s. The photodiode is followed by a 9 dB gain amplifier.

In the two preceding examples, the Fourier analysis of the signals delivered by the interferometer has allowed us to measure the different noise affecting the frequency of our chirped laser, but only *a posteriori*. The orders of magnitude of the different errors we have observed permit us to conclude that if we want to reach a precision better than, say, 1 MHz over the laser frequency during the chirp, we have to take care of the possible deterministic frequency errors, either periodic or not, and of the low-frequency component of the stochastic frequency noise. The white frequency noise has been shown to lead to a Lorentzian broadening of the order of 10 kHz and can be ignored [96]. Consequently, all the frequency

noise we have to deal with for our RF spectral analysis applications using rare earth ion doped crystals exhibit bandwidths lying below 1 MHz. This is within the range of conventional electronic servo control loops and one would be tempted to servo-lock the laser chirp to a perfect linear chirp within an error smaller than 1 MHz. However, to realize this, we need to measure the laser frequency instantaneously. This can be performed using our interferometer, provided that we measure the phase difference $\Psi$ between the two arms at the output of the interferometer.

This phase can be obtained provided we detect two signals in quadrature at the output of the interferometer [97] using two photodiodes. In general, the phase difference between these two signals and the equality of their amplitudes can be adjusted by tuning the orientations of a quarter-wave plate and a half-wave plate located at the output of the fiber, together with one polarizer in front of each detector. Here we simply use one half-wave plate at the output of the fiber. The rotation of this half-wave plate allows us to perfectly adjust the $\pi/2$ dephasing between the two signals, even if their amplitudes cannot be equalized. Some resulting typical signals are reproduced in Figure 27(a). They were obtained with a 20-m-long fiber, corresponding to $\tau_d = 100$ ns, with a chirp rate $r = 1.6$ GHz/ms ($\Delta\nu_{laser} = 6.4$ GHz in $T = 4$ ms). Since a $2\pi$ dephasing of the interferometer corresponds to a frequency variation of $1/\tau_c = 10$ MHz, reaching a precision better than 1 MHz on the laser frequency requires one to measure $\Psi$ with a resolution better than $\pi/5$. Figure 27(a) shows that this is easily achieved with the sampling rate of 6.25 MHz that we use. The phase error $\delta\Psi(t) = \Psi(t) - 2\pi r \tau_d t$ induced by the laser frequency error can easily be reconstructed from the two quadrature signals, as evidenced in Figure 27(b). This signal contains the different types of errors we have observed. It is the superposition of i) a quasi-linear drift, ii) a sinusoidal modulation, and iii) a stochastic component.

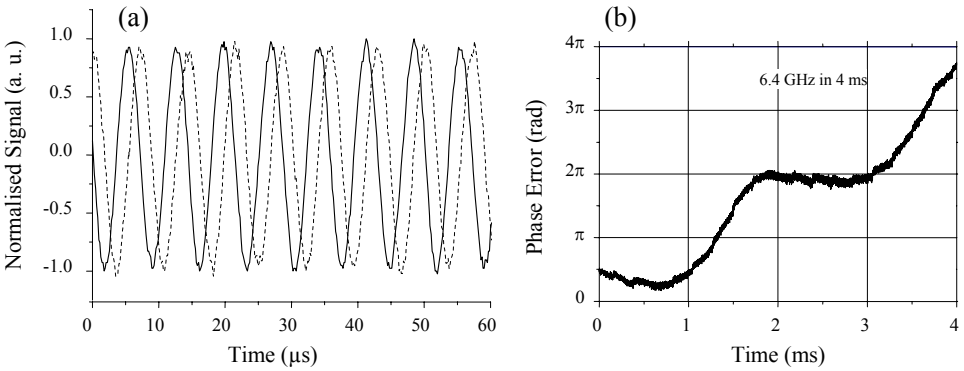


Figure 27. (a) Quadrature signals measured at the output of the interferometer for $\tau_d$ = 100 ns and $r$ = 1.6 GHz/ms. This figure reproduces only a small portion of the record. (b) Corresponding phase error. The sampling rate of the digital oscilloscope is 6.25 MHz.

Such a signal could be filtered and used as an error signal to lock the laser frequency in a digital servo loop with a correction voltage applied on the electro-optic crystal, as already used for a fixed frequency laser [86]. As we have seen above, all the errors we have to correct for, i.e., the deterministic frequency errors and the low-frequency part of the stochastic noise, lie in a bandwidth smaller than a few hundreds of kHz. A loop bandwidth of 1 MHz would consequently be sufficient. Besides, each interference fringe of Figure 27(a) corresponds to a variation of the laser frequency of $1/\tau_d$ = 10 MHz. Consequently, a resolution better than 1 MHz, as required for spectral analysis applications, could easily be achieved by digitalizing the quadrature signals with 8-bit converters.

## 7.4. Perspectives

While the laser model described in section 7.2 proved efficient in the demonstration of the rainbow and the photographic analyzers, frequency agile laser technology must be improved. From an application point of view, the model is too big, heavy, and sensitive to external perturbations. In addition, the high voltage source requirement limits the chirp speed, is a source of noise, and consumes electrical power. Also, the chirp linearity must still be improved, especially for high bandwidth operation of the chirp transform analyzer.

We are pursuing two paths for achieving these goals. One consists in developing more compact and lightweight laser structures, the other in working out efficient schemes for opto-electronic control of the laser chirp purity.

In collaboration with the team of Pr.W. Sohler from Paderborn University, we have recently designed an extended cavity diode laser whose light is coupled into a monomode waveguide inscribed in a LiNbO3 wafer by titanium indiffusion [98]. The cavity is closed by a Bragg grating, holographically written via the photorefractive effect in a Fe doped section of the waveguide. This approach leads to a very compact design which could be made monolithic. Also, the waveguide approach considerably increases the electro-optic frequency tuning sensitivity since the electrode spacing is reduced to about 10µm instead of 1mm for the unguided laser cavities described in section 7.2. A sensitivity of 55 MHz/V was obtained, which could be increased by a factor of 5 with a different crystal cut.

Active stabilization of the laser chirps is also under study. Analog and digital high bandwidth phase locked loops are under development to lock the frequency chirp to a Mach-Zehnder interferometer, along the lines discussed in Section 7.3. These are derived from the low bandwidth frequency locking loop developed by Juncar and Pinard [97]. We believe these should yield laser frequency chirps whose beat note linewidth is limited by the inverse chirp duration.

# 8. Conclusion

As illustrated by these few examples, hybridization of fast electronic with atomic and laser physics appears to be a powerful tool for broadband signal processing. The proposed RF spectral analysis architectures offer unrivaled capabilities in terms of instantaneous bandwidth, number of frequency channels, and probability of interception. The spectrum photography configuration has already demonstrated 10GHz instantaneous bandwidth with 10000 channel capacity. The rainbow analyzer, by offering simultaneous access to the

different spectral channels, is well suited for long time spectral integration. As for the photon echo chirp transform architecture, its coherent coverage of the bandwidth guarantees Fourier transform limited access time to the spectral addresses. To meet the requirements in terms of stability, scanning speed, range and repeatability, original tunable lasers have been developed together with specific diagnostic, monitoring and control techniques. Integrated cryogenics now represents the next important milestone on the roadmap to a demonstrator assembly. However mechanical cryocoolers have accomplished dramatic progress in recent years, stimulated by development initiatives such as the NASA's Advanced Cryocooler Technology Development Program. Multistage refrigerators, able to offer a few milliwatts cooling power at 5K, starting from room temperature, should not exceed 20kg payload and 200Watts input power [99].

**Acknowledgments**

The authors are much indebted to the many collaborators who took part in the development of atomic RF spectral analyzers. Among them, the PhD students L. Ménager, V. Lavielle, V. Crozatier, and G. Gorju deserve special acknowledgments of their contributions. Discussions with J.-P. Huignard, D. Dolfi, I. Zayer, K. Wagner, S. Tonda, L. Morvan, F. Schlottau, L. Levin were very motivating and enriching. The help of T. Böttger, R. Equall and Y. C. Sun was invaluable in the understanding of the erbium crystal parameters. We gratefully acknowledge support from European Space Agency under contracts ESTEC/12876/98/NL/MV and ESTEC/14174/00/NL/SB, from Délégation Générale de l'Armement under contract DGA STTC/34047 and from the NICOP Program of the Office of Naval Research under contract N00014-03-10770.

## REFERENCES


[1] A. Szabo, “Observation of the Optical Analog of the Mössbauer Effect in Ruby”, Phys. Rev. Lett. **27**, 323-326 (1971).

[2] A. Szabo, “Frequency selective optical memory”, US patent 3 896 420 (22 July 1975).

[3] G. Castro, D. Haarer, R. M. Macfarlane, H. P. Trommsdorff, “Frequency selective optical data storage system”, US patent 4 101 976 (18 July 1978).

[4] A. A. Gorokhovskii, R. K. Kaarli, L. A. Rebane, “Hole burning in the contour of a pure electronic line in a Shpol’skii system”, JETP Lett. **20**, 216-218 (1974).

[5] B. M. Kharlamov, R. I. Personov, L. A. Bykovskaya, “Stable "gap" in absorption spectra of solid solutions of organic molecules by laser irradiation”, Opt. Commun. **12**, 191-193 (1974).

[6] B. Kohler, S. Bernet, A. Renn, U. P. Wild, “Storage of 2000 holograms in a photochemical hole-burning system”, Opt. Lett. **18,** 2144-2146 (1993).

[7] E. S. Maniloff, S. B. Altner, S. Bernet, F. R. Graf, A. Renn, U. P. Wild, “Recording of 6000 holograms by use of spectral hole burning”, Appl. Opt. **34**, 4140-4148 (1995).

[8] B. Plagemann, F. R. Graf, S. B. Altner, A. Renn, U. P. Wild, “Exploring the limits of optical storage using persistent spectral hole-burning : holographic recording of 12000 images”, Appl. Phys. B **66**, 67-74 (1998).

[9] A. Renn, U. P. Wild, A. Rebane, “Multidimensional Holography by Persistent Spectral Hole Burning”, J. Phys. Chem. A **106**, 3045-3060 (2002).

[10] T. W. Mossberg, “Time-domain frequency-selective optical data storage”, Opt. Lett. **7**, 77-79 (1982).

[11] T. W. Mossberg, “Swept-carrier time-domain optical memory”, Opt. Lett. **17**, 535-537 (1992).

[12] H. Lin, T. Wang, G. A. Wilson, T. W. Mossberg, “Experimental demonstration of swept-carrier time-domain optical memory”, Opt. Lett. **20**, 91-93 (1995).

[13] H. Lin, T. Wang, T. W. Mossberg, “Demonstration of 8-Gbit/in.² areal storage density based on swept-carrier frequency selective optical memory”, Opt. Lett. **20**, 1658-1660 (1995).

[14] Z. Cole, T. Böttger, R. Krishna Mohan, R. Reibel, W. R. Babbitt, R. L. Cone, K. D. Merkel, “Coherent integration of 0.5 GHz spectral holograms at 1536 nm using dynamic biphase codes”, Appl. Phys. Lett. **81**, 3525-3527 (2002).

[15] K. D. Merkel, W. R. Babbitt, “Optical coherent-transient true-time-delay regenerator”, Opt. Lett. **21**, 1102-1104 (1996).

[16] K. D. Merkel, Z. Cole, W. R. Babbitt, “Signal correlator with programmable variable time delay based on optical coherent transients”, J. Lumin. **86**, 375-382 (2000).

[17] R. Reibel, Z. Barber, M. Tian, W. R. Babbitt, “Temporally overlapped linear frequency-chirped pulse programming for true-time-delay applications”, Opt. Lett. **27**, 494-496 (2002).

[18] M. R. Schoeberl, A. R. Douglass, E. Hilsenrath, P. K. Bhartia, J. Barnett, J. Gille, R. Beer, M. Gunson, J. Waters, P. F. Levelt and P. DeCola, “The EOS Aura Mission”, EOS, Transactions, American Geophysical Union **85,** 177-184 (2004).

[19] J. W. Waters, W. G. Read, L. Froidevaux, R. F. Jarnot, R. E. Cofield, D. A. Flower, G. K. Lau, H. M. Pickett, M. L. Santee, D. L. Wu, M. A. Boyles, J. R. Burke, R. R. Lay, M. S. Loo, N. J. Livesey, T. A. Lungu, G. L. Manney, L. L. Nakamura, V. S. Perun, B. P. Ridenoure, Z. Shippony, P. H. Siegel and R. P.Thurstans, “The UARS and EOS Microwave Limb Sounder (MLS) Experiments”, J. Atmos. Sci. **56**, 194-218 (1998).

[20] J. W. Waters, “An Overview of the EOS MLS Experiment”, JPL D-15745, Version 1.0 (1999).

[21] R. F. Jarnot, "EOS MLS Level 1 Data Processing Algorithm Theoretical Basis", JPL D-15210, Version 1.1 (1999).
[22] N. Kaifu, N. Ukita, Y. Chikada, T. Miyaji, "A High-Resolution Acousto-Optical Radiospectrometer for Millimeter-Wave Astronomy", Publ. Astron. Japan **29**, 429-435 (1977).
[23] T. W. Cole, D. K. Milne, "An Acousto-Optical Radio Spectrograph for Spectral Integration", *Proc. of Astronomical Society of Australia*, 30 May – 01 June 1977, Clayton, Australia, ASA **3**, 108-111 (1977).
[24] M. Klumb, J. Frerick, R. Schieder, G. Winnewisser, V. Tolls, "The SWAS Acousto Optical Spectrometer", *Proc. of Infrared Spaceborne Remote Sensing II*, July 27-29 1994, San Diego, California, ed. M. S. Scholl, Proceedings of the SPIE **2268**, 305-315 (1994).
[25] V. Tolls, G. J. Melnick, N. Erickson, P. Goldsmith, M. Harwit, R. Schieler, R. Snell, J. R. Stauffer, "The Submillimeter Wave Astronomy Satellite – The Instrument", *Proc. of The Physics and Chemistry of Interstellar Molecular Clouds*, Sept. 21-24 1993, Zermatt, Switzerland, eds. G. Winnewisser and G. C. Pelz, Springer-Verlag, Lect. Notes in Phys. **459** (1995).
[26] G. J. Melnick, J. R. Stauffer, M. L. N. Ashby, E. A. Bergin, G. Chin, N. R. Erickson, P. F. Goldsmith, M. Harwit, J. E. Howe, S. C. Kleiner, D. G. Koch, D. A. Neufeld, B. M. Patten, R. Plume, R. Schieder, R. L. Snell, V. Tolls, Z. Wang, G. Winnewisser, Y. F. Zhang, "The Submillimeter Wave Astronomy Satellite: Science Objectives and Instrument Description", The Astrophysical Journal **539**, 77-85 (2000).
[27] U. Frisk, M. Hagström, J. Ala-Laurinaho, S. Andersson, J.-C. Berges, J.-P. Chabaud, M. Dahlgren, A. Emrich, H.-G. Florén, G. Florin, M. Fredrixon, T. Gaier, R. Haas, T. Hirvonen, Å. Hjalmarsson, B. Jakobsson, P. Jukkala, P. S. Kildal, E. Kollberg, J. Lassing, A. Lecacheux, P. Lehikoinen, A. Lehto, J. Mallat, C. Marty, D. Michet, J. Narbonne, M. Nexon, M. Olberg, A. O. H. Olofsson, G. Olofsson, A. Origné, M. Petersson, P. Piironen, R. Pons, D. Pouliquen, I. Ristorcelli, C. Rosolen, G. Rouaix, A. V. Räisänen, G. Serra, F. Sjöberg, L. Stenmark, S. Torchinsky, J. Tuovinen, C. Ullberg, E. Vinterhav, N. Wadefalk, H. Zirath, P. Zimmermann and R. Zimmermann, "The Odin satellite", A&A **402**, L27-L34 (2003).
[28] A. Lecacheux, C. Rosolen, D. Michet, V. Clerc, "Space Qualified, Wide Bandand Ultra Wide Band Acousto-Optical Spectrometers for Millimeter and Sub-Millimeter Radio Astronomy", *Proc. of Advanced Technology MMW, Radio, and Terahertz Telescopes* conference, March 20-28 1998, Kona, Hawaii, USA, ed. T. G. Phillips, Proceedings of the SPIE **3357**, 519-532 (1998).
[29] G. L. Pilbratt, "The Herschel Mission, Scientific Objectives, and this Meeting", *Proc. of The Promise of the Herschel Space Oservatory* symposium, 12-15 décembre 2000, Toledo, Spain, eds. G. L. Pilbratt, J. Cernicharo, A. M. Heras, T. Prusti, R. Harris, ESA **SP-460**, 21-27 (2001).
[30] J. Horn, "The development of an array acousto-optical spectrometer", PhD thesis, Köln University (1997).
[31] J. Horn, O. Siebertz, F. Schmülling, C. Kunz, R. Schieder, G. Winnewisser, "A 4x1 GHz Array Acousto-Optical Spectrometer", Exp. Astron. **9**, 17-38 (1999).
[32] R. Schieder, J. Horn, O. Siebertz, C. Möckel, F. Schlöder, C. Macke, F. Schmülling, "Design of Large Bandwidth Acousto-Optical Spectrometers", *Proc. of Advanced Technology MMW, Radio, and Terahertz Telescopes* conference, March 20- 28 1998, Kona, Hawaii, USA, ed. T. G. Phillips, Proceedings of the SPIE **3357**, 359-367 (1998).
[33] A. R. Thompson, J. M. Moran, G. W. Swenson, "Interferometry and Synthesis in Radio Astronomy", Wiley, Ch. 8, 1986.

[34] T. Cole, “Finite Sample Correlations of Quantized Gaussians”, Aust. J. Phys. **21**, 273-282 (1968).
[35] A. Emrich, “Autocorrelation Spectrometers for Space Borne (Sub)millimeter Spectroscopy”, *Proc. of The Far InfraRed and Submillimeter Universe* symposium, Apr. 15-17 , 1997, Grenoble France, ESA **SP-401**, 361-364 (1997).
[36] A. I. Harris, “Spectrometers for Heterodyne Detection”, *Proc. of Far-IR, Sub-mm & mm Detector Technology Workshop*, 01-03 avril 2002, Monterey, California, USA, eds. J. Wolf, J. Farhoomand, C. R. McCreight, NASA/**CP-211408** (2002).
[37] L. Ravera, M. Giard, D. Lagrange, E. Caux, A. Cros, G. Serra, J.-L. Noullet, A. Ferreira, P. Cais, A. Baudry, J. M. Desbat, A. Escobar, G. Montignac, M. Torres, J. Y. Mayvial, “Wideband digital autocorrelator for FIRST”, *Proc. of Advanced Technology MMW, Radio, and Terahertz Telescopes* conference, 20-28 mars 1998, Kona, Hawaii, USA, ed. T. G. Phillips, Proceedings of the SPIE **3357**, 368-375 (1998).
[38] T. de Graauw, F. P. Helmich, “Herschel-HIFI : The Heterodyne Instrument for the Far-Infrared”, *Proc. of The Promise of the Herschel Space Observatory* symposium, 12-15 December 2000, Toledo, Spain, eds. G. L. Pilbratt, J. Cernicharo, A. M. Heras, T. Prusti, R. Harris, ESA **SP-460**, 45-51 (2001).
[39] A. I. Harris, K. G. Isaak, J. Zmuidzinas, “WASP: A wideband spectrometer for heterodyne spectroscopy”, *Proc. of Advanced Technology MMW, Radio, and Terahertz Telescopes* conference, 20-28 March 1998, Kona, Hawaii, USA, ed. T. G. Phillips, Proceedings of the SPIE **3357**, 384-395 (1998).
[40] A. I. Harris, J. Zmuidzinas, “A wideband lag correlator for heterodyne spectroscopy of broad astronomical and atmospheric spectral lines”, Rev. Sci. Inst. **72**, 1531-1538 (2001).
[41] L. I. Bluestein, A linear filtering approach to the computation of the discrete Fourier transform. IEEE Trans. Electroacoustics AU-18, 451–455 (1970).
[42] H. R. Fetterman, P. E. Tannenwald, C. D. Parker, J. Melngailis, R. C. Williamson, P. Woskoboinikow, H. C. Praddaude et W. J. Mulligan, “Real-time spectral analysis of far-infrared laser pulses using SAW dispersive delay line”, Appl. Phys. Lett. **34**, 123-125 (1979).
[43] P. Hartogh et G. K. Hartmann, “A high-resolution chirp transform spectrometer for microwave measurements”, Meas. Sci. Technol. **1**, 592-595 (1990).
[44] R. Güsten, I. Camara, P. Hartogh, H.-W. Hübers, U. Graf, K. Jacobs, C. Kasemann, H.-P. Röser, R. Schieder, G. Schnieder, O. Siebertz, J. Stutzki, G. Villanueva, A. Wagner, P. van der Wal et A. Wunsch, “GREAT: The German Receiver for Astronomy at Terahertz Frequencies”, *Proc. of Airborne Telescope System II* conference, Aug. 27-28 2002, Waikoloa, Hawaii, USA, eds. R. K. Melugin et H.-P. Röser, Proceedings of the SPIE **4857**, 56-61 (2003).
[45] R. Güsten, F. Schäfer, R. Stark, P. van der Wal, U. Graf, R. Schieder, J. Stutzki, H. Hübers, A. Krabbe, H.-P. Röser et P. Hartogh, “The next step: FIR heterodyne spectroscopy on board SOFIA”, *ISO beyond the peaks: The 2nd ISO workshop on analytical spectroscopy*, Feb. 2-4 2000, satellite tracking station of Villafranca del Castillo, Spain, ed. D. Danesy, ESA **SP-456** (2000).
[46] R. Güsten, P. Hartogh, H.-W. Hübers, U. Graf, K. Jacobs, H.-P. Röser, F. Schäfer, R. Schieder, R. Stark, J. Stutzki, P. van der Wal, A. Wunsch, “GREAT – The First-Generation German Heterodyne Receiver For SOFIA”, *Proc.of Airborne Telescope Systems*, March 27-28 2000, Munich, Germany, eds. R. K. Melugin, H.-P. Röser, Proceedings of the SPIE, **4014**, 23-30 (2000).
[47] G. Villanueva, P. Hartogh, L. Reindl, “Microwave Technologies for SOFIA’s High Resolution Spectrometer”, *Proc. of The 33rd European Microwave Conference*, 6-10 Oct. 2003, Munich, Germany, **3** (2003).

[48] M. Colice, F. Schlottau, K. Wagner, K. Mohan, W. R. Babbitt, I. Lorgeré, and J.-L. Le Gouët, "RF spectrum analysis in spectral hole burning media," in *Proc. SPIE (Optical Information Systems II)*, vol. **5557**, 132-139 (2004).
[49] R. K. Mohan, Z. Cole, R. R. Reibel, T. Chang, K. D. Merkel, W. R. Babbitt, M. Colice, F. Schlottau, and K. H. Wagner, "Microwave spectral analysis using optical spectral holeburning," in *Proc. Microwave Photonics (MWP),* Ogunquit, MA, Oct. 2004.
[50] J.-L. Le Gouët, I. Lorgeré, F. Bretenaker, V. Lavielle, and V. Crozatier, "Atomic spectral analyzers for radio frequency signals processing," in *Proc. IEEE/LEOS Annual Meeting*, Puerto-Rico, Oct. 2004.
[51] G. Gorju, V. Crozatier, I. Lorgeré, J.-L. Le Gouët, and F. Bretenaker, "10-GHz Bandwidth RF Spectral Analyzer with MHz Resolution Based on Spectral Hole Burning in $Tm^{3+}$:YAG," IEEE Photonics Technology Letters **17**, 2385-2387 (2005).
[52] F. Schlottau, M. Colice, K. H. Wagner, and W. R. Babbitt, "Spectral hole burning for wideband, highresolution radio-frequency spectrum analysis," Optics Letters **30**, 3003-3005 (2005).
[53] R.M. Macfarlane, T.L. Harris, Y. Sun, R.L. Cone, R.W. Equall, « Measurement of photon echoes in Er:$Y_2SiO_5$ at 1.5μm with a diode laser and an amplifier, » Opt. lett. **22** (1997) 871-873.
[54] T.L. Harris, Y. Sun, R.L. Cone, R.M. Macfarlane, R.W. Equall, « Demonstration of real-time address header decoding for optical data routing at 1536nm, » Opt. Lett. **23** (1998) 636-638.
[55] R.W. Equall, Y. Sun, R.L. Cone, R.M. Macfarlane, « Ultraslow optical dephasing in $Eu^{3+}$:$Y_2SiO_5$, » Phys. Rev. Lett. **72** (1994) 2179-2182.
[56] R.M. Macfarlane, « Spectral hole burning in the trivalent thulium ion, » Opt. Lett **18** (1993) 829-831.
[57] W. H. Hesselink, D.A. Wiersma, « Photon echoes stimulated from an accumulated grating: Theory of generation and detection, » J. Chem. Phys. **75** (1981) 4192-4197.
[58] L. Levin, « Mode-hop-free electro-optically tuned diode laser, » *Opt. Lett.,* vol 27, pp 237-239, Feb. 2002.
[59] L. Ménager, I. Lorgeré, J.-L. Le Gouët, « Fresnel diffraction on the edge of causality », Opt. Lett., **25,** 1313-1315, (2000).
[60] T. Chang, R. K. Mohan, M. Tian, T. L. Harris, W. R. Babbitt, and K. D. Merkel, « Frequency-chirped readout of spatial-spectral absorption features, » *Phys. Rev. A*, vol. 70, 063803, Dec. 2004.
[61] J. Poirson, F. Bretenaker, M. Vallet, and A. Le Floch, "Analytical and experimentally study of ringing effects in a Fabry-Perot cavity. Application to the measurement of high finesses," *J. Opt. Soc. Am.B*, vol. 14, pp. 2811-2817, Nov. 1997.
[62] G. Gorju, A. Chauve, I. Lorgeré, J.-L. Le Gouët, and F. Bretenaker, to be published.
[63] A. Rebane, R. Kaarli, P. Saari, A. Anijalg, and K. Timpmann, "Photochemical time-domain holography of weak picosecond pulses" Opt. Commun. **47**, 173-176 (1983).
[64] Y. Sun, C.W. Thiel, R.L. Cone, R.W. Equall, R.L. Hutcheson, « Recent progress in developing new rare earth materials for hole burning and coherent transient applications, » J. of Lumin. **98** (2002) 281-287.
[65] F. Schlottau and K. Wagner, « Demonstration of a continuous scanner and time-integrating correlator using spatial-spectral holography, » J. Lumin. 107 (2004) 90-102.
[66] I. Lorgeré, L. Ménager, V. Lavielle, J.-L. Le Gouët , D. Dolfi, S. Tonda and J.-P. Huignard, « Demonstration of a radio-frequency spectrum analyser based on spectral hole burning, » J. of Mod. Opt. 49 (2002) 2459-2475.

[67] S. Bernet, S. B. Altner, F. R. Graf, E. S. Maniloff, A. Renn, U. P. Wild, « Frequency and phase swept holograms in spectral hole-burning materials, » Appl. Opt. 34 (1995) 4674.
[68] V. Lavielle, I. Lorgeré, J.-L. Le Gouët, « Dispersion Only Stimulated Photon Echo, » Opt. Commun. 232 (2004) 263-271.
[69] V. Lavielle, I. Lorgeré, and J.-L. Le Gouët, S. Tonda and D. Dolfi, « Wideband versatile radio-frequency spectrum analyzer, » Opt. Lett. **28** (2003) 384-386.
[70] L. Ménager, L. Cabaret, I. Lorgeré, J.-L. Le Gouët, "Diode laser extended cavity for broadrange fast ramping", Opt. Lett., **25,** 1246-1248, (2000).
[71] U. Elman, B. Luo, S. Kröll, "Influence of laser phase and frequency fluctuations on photon-echo data erasure," J. Opt. Soc. Am. B **13** (1996) 1905-1915.
[72] K. D. Merkel, W. R. Babbitt, , "Optical coherent transient continuously programmed continuous processor," Opt. Lett. **24** (1999) 172-174.
[73] V. Lavielle, F. De Seze, I. Lorgeré, J.-L. Le Gouët, « Wideband radio frequency spectrum analyzer: improved design and experimental results, » J. Lumin. **107** (2004) 75-89
[74] T. Jannson, « Real time Fourier transformation in dispersive optical fibers", Opt. Lett., **8**, 232, (1983).
[75] B. H. Kolner, « Space time duality and the theory of temporal imaging, » IEEE J. Quant. Elect., **30,** 1951-1963, (1994).
[76] M. A. Jack, P. M. Grant and J. H. Collins, « The theory design and applications of surface acoustic wave Fourier transform processors, » Proc. IEEE, **68,** 450-468, (1980).
[77] See product line of e.g. Phonon Corporation, Temex Microsonics.
[78] R. R. Reibel, Z. W. Barber, J. A. Fisher, M. Tian and W. R. Babbitt, « Broadband demonstration of true time delay using linear sideband chirped programming and optical coherent transients, » J. Lum., **107,** 103-113, (2004).
[79] L. Ménager, J.-L. Le Gouët and I. Lorgeré, « Time to Frequency Fourier transform with photon echoes, » Opt. Lett., **26,** 1397-1399, (2001).
[80] H. Lin and T. Wang and G. A. Wilson and T. W. Mossberg, « Experimental demonstration of swept carrier time-domain optical memory, » Opt. Lett., **20,** 91-93, (1995).
[81] T. Böttger, « Laser frequency stabilization to spectral hole burning references in Er doped crystals: materials and optimization, » PhD Thesis, Montana State University, (2002).
[82] T. Böttger, Y. C. Sun, C. W. Thiel, R L. Cone, « Material Optimization of $Er^{3+}$:$Y_2SiO_5$ at at 1.5 μm for optical processing, memory, and laser frequency stabilization applications, » SPIE Proceedings of Advanced Optical Data Storage (OE05) (2003).
[83] A. Messiah, « Mécanique Quantique 2, » Dunod, Paris, (1964).
[84] Y. C. Sun, Private communication.
[85] V. Crozatier, G. Gorju, F. Bretenaker, J.-L. Le Gouët, I. Lorgeré, « High resolution radio frequency spectral analysis with photon echo chirp transform in a Er : YSO Crystal, » IEEE J. Quant. Elect., **40,** 1450-1457, (2004).
[86] V. Crozatier, F. de Seze, L. Haals, F. Bretenaker, I. Lorgeré, and J.-L. Le Gouët, « Laser diode stabilisation for coherent driving of rare earth ions, » Opt. Commun. **241**, 203-213 (2004).
[87] R.W.P. Drever, J.L. Hall, F.V. Kowalski, J. Hough, G.M. Ford, A.J. Munley and H. Ward, "Laser phase and frequency stabilization using an optical resonator," Appl. Phys. B **31**, 97-105 (1983).
[88] M. P. van Exter, S. J. Kuppens, J. P. Woerdman, "Excess phase noise in self-heterodyne detection," IEEE J. Quantum Electron. **28**, 580-584 (1992).

[89] L. E. Richter, H. I. Mandelberg, M. S. Kruger, P. A. McGrath, "Linewidth determination from self-heterodyne measurements with subcoherence delay times," IEEE J. Quantum Electron. **22**, 2070-2074 (1986)
[90] P. B. Gallion, G. Debarge, "Quantum phase noise and field correlation in single frequency semiconductor laser systems," IEEE J. Quantum Electron. **20**, 343-349 (1984).
[91] C. J. Karlsson, F. A. Olsson, "Linearization of the Frequency Sweep of a Frequency-Modulated Continuous-Wave Semiconductor Laser Radar and the Resulting Ranging Performance," Appl. Opt. **38**, 3376-3386 (1999).
[92] K. Repasky, and J. L. Carlsten, "Simple method for measuring frequency chirps with a Fabry-Perot interferometer," App. Opt. **39**, 5500-5504 (2000)
[93] C. Greiner, B. Boggs, T. Wang, and T. W. Mossberg, "Laser frequency stabilization by means of optical self-heterodyne beat-frequency control," Opt. Lett. **23**, 1280-1282 (1998).
[94] B. Boggs, C. Greiner, T. Wang, H. Lin, T.W. Mossberg, "Simple high-coherence rapidly tunable external-cavity diode laser," Opt. Lett. **23**, 1906-1908 (1998).
[95] S. Kakuma, K. Ohmura, R. Ohba, "Improved uncertainty of optical frequency domain reflectometry based length measurement by linearizing the frequency chirping of a laser diode," Opt. Rev. **10**, 182-184 (2003).
[96] G. Gorju, V. Crozatier, V. Lavielle, I. Lorgeré, J.-L. Le Gouët, and F. Bretenaker, "Experimental investigation of deterministic and stochastic frequency noises of a rapidly frequency chirped laser," Eur. Phys. J. Appl. Phys. **30**, 175-183 (2005).
[97] P. Juncar, J. Pinard, "Instrument to measure wave numbers of cw and pulsed laser lines: the sigmameter," Rev. Sci. Instrum. **53**, 939-948 (1982).
[98] V. Crozatier, B. K. Das, G. Baïli, G. Gorju, F. Bretenaker, J.-L. Le Gouët, I. Lorgeré, and W. Sohler, “Highly coherent electronically tunable waveguide extended cavity diode laser, » submitted.
[99] R.G. Ross, Jr., R. F. Boyle, R. W. Key and D. R. Coulter, « NASA advanced cryocooler technology development program, » Proceedings of the SPIE, **4850** 1020-8, The-International Society for Optical Engineering (2003).